Optimal Inlet Shape Design of N2B Hybrid Wing Body Configuration

Hyoungjin Kim*
Science Applications International Corporation, Cleveland, OH 44135
and
Meng-Sing Liou†
NASA Glenn Research Center, Cleveland, OH 44135

ABSTRACT

The N2B hybrid wing body aircraft was conceptually designed to meet environmental and performance goals for the N+2 generation transport set by the Subsonic Fixed Wing project of NASA Fundamental Aeronautics Program. In the present study, flow simulations are conducted around the N2B configuration by a Reynolds-averaged Navier-Stokes flow solver using unstructured meshes. Boundary conditions at engine fan face and nozzle exhaust planes are provided by the NPSS thermodynamic engine cycle model. The flow simulations reveal challenging design issues arising from boundary layer ingestion offset inlet and airframe-propulsion integration. Adjoint-based optimal designs are then conducted for the inlet shape to minimize the airframe drag force and flow distortion at fan faces. Design surfaces are parameterized by NURBS, and the cowl lip geometry is modified by a spring analogy approach. By the drag minimization design, flow separation on the cowl surfaces are almost removed, and shock wave strength got remarkably reduced. For the distortion minimization design, a circumferential distortion indicator $DPCP_{avg}$ is adopted as the design objective and diffuser bottom and side wall surfaces are perturbed for the design. The distortion minimization results in a 12.5 % reduction in the objective function.

Nomenclature

ADP = Aerodynamic Design Point
AIP = Aerodynamic Interface Plane
AOA = Angle of Attack
BLI = Boundary Layer Ingestion
BPR = Bypass Ratio
C_L,C_D, C_T = Aircraft lift, drag and thrust coefficients
C_p = Pressure coefficient
HWB = Hybrid Wing Body aircraft
ISA = International Standard Atmosphere
M = Mach number
$\dot{m}$ = Mass flow rate
NPSS = Numerical Propulsion System Simulation
OML = Outer Mold Line
OPR = Overall Pressure Ratio
P_t, T_t = Total pressure, total temperature
SFC = Specific Fuel Consumption
SFW = Subsonic Fixed Wing
SLS = Sea Level Static
TOC = Top of Climb

* Aerospace Engineer, Senior Member AIAA
† Senior Technologist, Associate Fellow AIAA

u, v = parametric space coordinates
x, y, z = Cartesian coordinates
η = Mass-weighted average total pressure recovery at fan face

I. Introduction

The Subsonic Fixed Wing (SFW) project of NASA Fundamental Aeronautics Program has focused on research of next generations of civil aircraft. For each time frame of near-, mid- and long-term periods, specific reduction goals in noise, emission, and fuel burn was defined from the current state of the art of aviation technology [1] as shown in Table 1. To achieve the aggressive goals especially for the N+2 and N+3 time frames, innovative design concepts in airframe and propulsion need to be explored.

Table 1 NASA subsonic fixed wing project goals [1]

TECHNOLOGY BENEFITS*	TECHNOLOGY GENERATIONS (Technology Readiness Level = 4-6)		
	N+1 (2015)	N+2 (2020**)	N+3 (2025)
Noise (cum margin rel. to Stage 4)	-32 dB	-42 dB	-71 dB
LTO NOx Emissions (rel. to CAEP 6)	-60%	-75%	-80%
Cruise NOx Emissions (rel. to 2005 best in class)	-55%	-70%	-80%
Aircraft Fuel/Energy Consumption‡ (rel. to 2005 best in class)	-33%	-50%	-60%

* Projected benefits once technologies are matured and implemented by industry. Benefits vary by vehicle size and mission. N+1 and N+3 values are referenced to a 737-800 with CFM56-7B engines, N+2 values are referenced to a 777-200 with GE90 engines

** ERA's time-phased approach includes advancing "long-pole" technologies to TRL 6 by 2015

‡ CO_2 emission benefits dependent on life-cycle CO_{2e} per MJ for fuel and/or energy source used

The hybrid wing body (HWB) aircraft, although not new, is an alternative design concept to the conventional tube-and-wing aircraft [2]. It has the fuselage and wings integrated into a flying wing, which has better aerodynamic efficiency than the tube-and-wing type configuration. Also, the wide airframe body of HWB is beneficial for shielding downward-propagating noise from engines installed above the aircraft.

The Boeing Company conducted a conceptual design study of HWB configurations satisfying NASA SFW N+2 goals through a contract sponsored by NASA's SFW project of the Fundamental Aeronautics Program [3]. As a starting point, the "Silent Aircraft" SAX-40 [4, 5], a non-proprietary configuration was chosen. Two HWB configurations were considered in the study; one is the N2A model employing conventional podded engines and the other is the N2B model, which adopts embedded engines and boundary layer ingestion (BLI) offset inlets. The SAX-40, N2A and N2B configurations are illustrated in Fig.1. Figure 2 shows the embedded engine adopted in N2B having three fans and variable area thrust vectoring/reversing nozzles. Compared to conventional pylon-mounted engines, embedded engines with BLI offset inlets allow reduced ram drag, wetted area, structural weight, and noise. Disadvantages of the embedded engines are higher flow distortion and reduced pressure recovery at engine faces due to the BLI offset inlet.

Application of design optimization to BLI inlet shape design and flow control has been addressed by several researches. Allan et al. [6] conducted a Design-of-Experiment based shape design of a single row of vortex generator vanes to minimize circumferential distortion and first five half amplitude of harmonics and to maximize recovery at

AIP using CFD. They reported an 80% reduction of $DPCP_{avg}$, a circumferential distortion level and a decrease in recovery by more than 0.6% point at the AIP of the inlet A model for transonic flow conditions. Lee and Liou [7] applied an adjoint-based shape design optimization to the inlet A model adopting high density design parameters on the bottom surface near the inlet throat. The resulting design shape appears like a successive alternation of lateral bumps and grooves. They obtained not only a 52.5% reduction in the circumferential distortion but also a 3.3% increment in the total pressure recovery at AIP. Carter et al. [8] applied a knowledge-based inverse design method to a HWB configuration with a flow-through nacelle. Wing upper surface near the inlet entrance was redesigned to have better flow characteristics. Rodriguez [9] conducted a CFD-based design optimization study for BLI inlet shape design on a three-engine HWB configuration utilizing a complex variable method for calculation of objective function gradients.

High fidelity CFD based analysis/design is essential for accurate performance evaluation/improvement of propulsion-airframe integration of HWB configurations with embedded engines like N2B. In the present study, flow simulations of the N2B configuration is conducted to understand effects of propulsion–airframe integration on the flow field around the vehicle and the embedded engine. Then an adjoint-based optimal inlet shape design study is performed to improve aerodynamic and propulsive performances.

The remainder of this paper is organized as follows. In Section 2, the N2B configuration is reviewed and response surfaces for thermodynamic cycle models of the embedded engine are generated for boundary conditions. In Section 3, methodologies for the flow simulation and optimal shape design are explained including the flow solver, mesh generation, boundary conditions, sensitivity analysis and design parameterization. Simulation results for the N2B aircraft are presented in Section 4. Optimal shape design results are shown in Section 5. Summary and conclusions are then followed in Section 6.

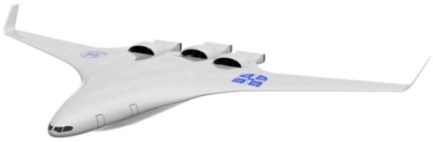

(a) SAX-40

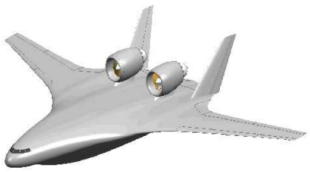

(b) N2A with podded engines

(c) N2B with embedded engines

(d) Top view of the HWB aircrafts

Fig. 1 HWB aircraft configurations [3]

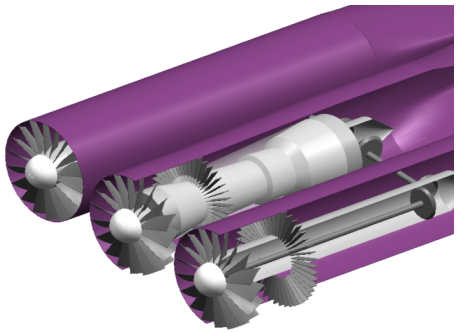

(a) Tri-fan + core engine

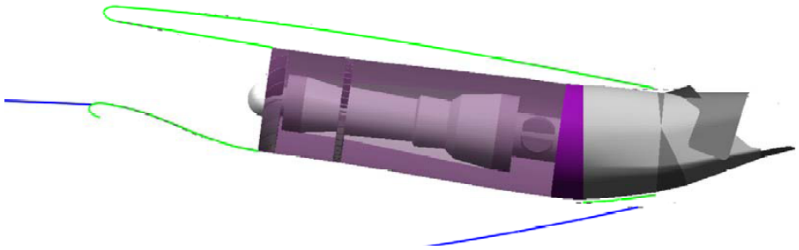

(b) Core engine + variable area thrust vectoring nozzle

Fig. 2. Multiple fan embedded turbofan engine for N2B [3]

II. N2B Hybrid Wing Body Aircraft

A. N2B specification [3]

N2B was suggested by Boeing as a cargo freighter aircraft and conceptually designed to have a 477,400 lb_m MTOGW, 103,000 lb_m payload and a 6,000 nm range. The cruise Mach number is 0.80 and initial cruise altitude is 31,000 ft. Time to climb 31,000 ft is 0.29 hour. The span length is 213 ft, and the reference area is 9246 ft^2. It has three engines, each of which has three fans and one core engine.

B. Engine model

Figure 3 shows the internal layout of the tri-fan embedded turbofan engine. The concept was based on the GRANTA engine of SAX-40 aircraft [5]. Conceptual design of the embedded engine was conducted at NASA Glenn Research Center for 2020 technology level [10]. Each engine has a gas generator (core engine) which drives an inline fan and two additional outboard fans through a mechanical transmission system. The Aerodynamic Design Point (ADP) is Mach number 0.8 and altitude of 31,000ft. The required thrust per engine at ADP is 10,000 lb at ISA+0. The design fan pressure ratio is 1.50 at ADP. All the fans are of the same diameter and rotate at the same speed. The design bypass ratio (BPR) of the core engine is 3.1 and overall effective BPR of the tri-fan engine is 11.3 at ADP. The fan face Mach number is 0.674. The fan efficiency was assumed to be degraded by one percent point due to the inlet flow distortion. The engine thermodynamic cycle was designed using the NPSS (Numerical Propulsion System Simulation) program [11,12] in the study of Ref. [6]. Some details of N2B embedded engine cycle information are given in Table 2.

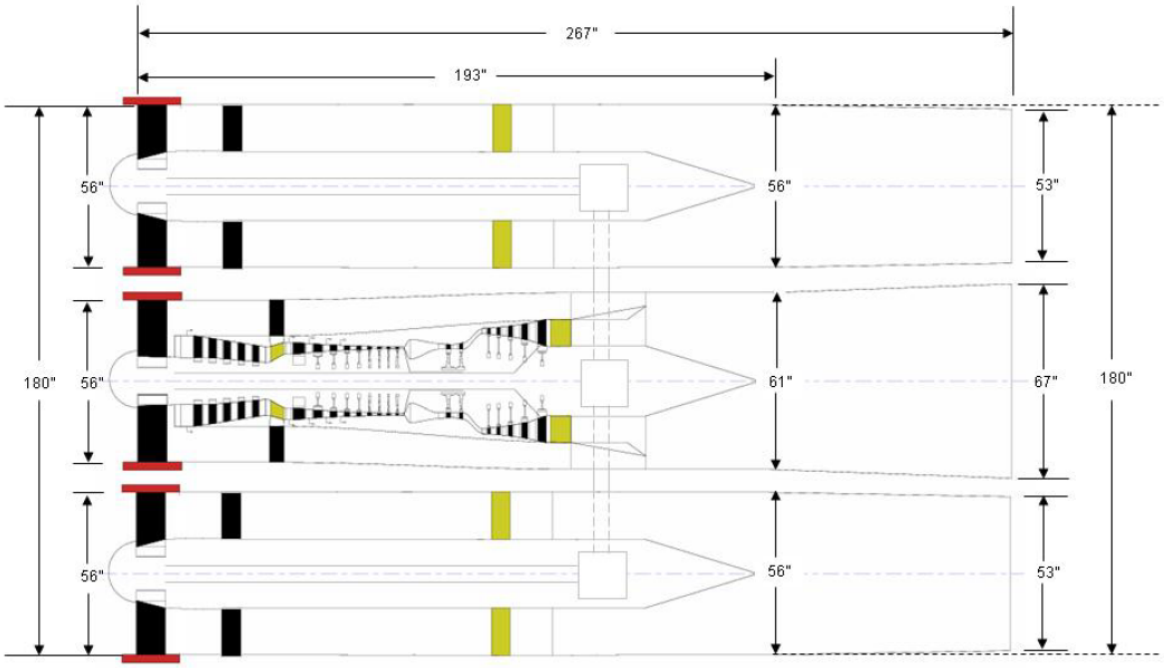

Fig.3 Internal layout of the embedded engine [10]

Table 2 NASA N2B embedded engine cycle information [3, 10]

	SLS (ISA+27°F)	ADP (M0.80/31kft/ISA+0°F)	TOC (M0.80/35kft/ISA+0°F)
Fan Pressure Ratio (FPR)	1.49	1.50	1.50
BPR (core engine + central fan only)	3.2	3.1	3.1
Effective BPR (3 fans)	11.5	11.3	11.3
Overall Pressure Ratio (OPR)	45	46	46
Net thrust per engine, lb	49060	10000	8286
SFC, lb/(lb-hr)	0.288	0.564	0.553
HPT inlet temperature (T4), °R	3460	3010	2920
HPT rotor inlet temperature (T41), °R	3310	2876	2789
LPT rotor inlet temperature (T49), °R	2460	2113	2044

Total pressure recovery values at engine fan faces at the ADP condition are estimated by Boeing from the mass averaged total pressure recovery of the inlet capture flow at the inlet highlight using RANS flow analysis results for a clean wing configuration. A usage of fixed vane vortex generators was supposed to mitigate inlet distortion, and inlet diffuser loss was assumed to be 0.6% [3]. The recovery values are 0.96705 for side fans and bypass flow for the center passage and 1.0 for core flow of the center passage assuming that uncontaminated flow is fed into the core engine, while the boundary layer flow is ingested into the two side fans and the bypass flow of the central passage. The engine thermodynamic cycle design was conducted based on the recovery values at the ADP condition.

In the present study for computational fluid dynamics simulations of the N2B configuration, the embedded turbofan engines are replaced with an NPSS engine model as illustrated in Fig.4. Total pressure recoveries at engine fan faces are calculated by CFD and provided to the NPSS model and engine boundary conditions required by CFD simulations are obtained from the NPSS model as shown in Fig.4(c).

In the flow simulation, an engine fan face is treated as a subsonic exit boundary condition with a specified target mass flow rate, which is matched by adjusting a uniform static back pressure. And a nozzle exhaust plane is treated as a subsonic inflow boundary condition with specified total conditions and a mass flow rate.

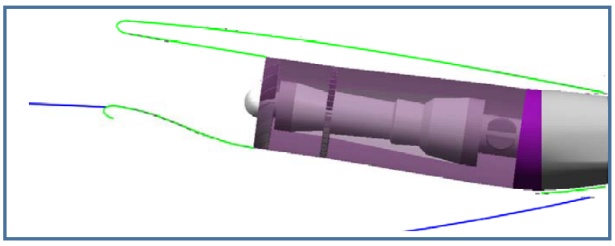

(a) Section view of the embedded engine core path.

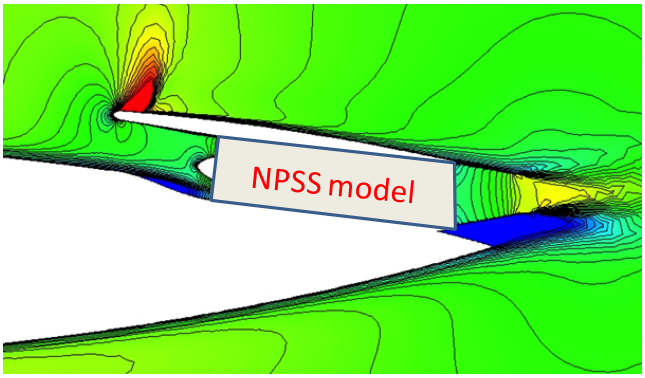

(b) Replacement of the engine with NPSS model.

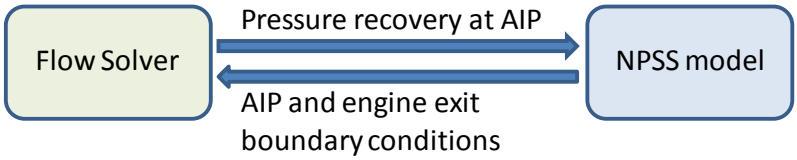

(c) Coupling of flow solver and NPSS model.

Fig. 4 Engine boundary conditions by NPSS model

In actual implementation, the coupling of the NPSS model with the flow solver can be made in a direct way by integrating the flow solver with the NPSS program via a script file for exchanging data of the two codes. An alternative choice is to build algebraic response surface models for the engine cycle and inserting the algebraic models into the flow solver [13]. In the present study, we employ the response surface approach for simplicity of the coupling. Accuracy of the coupling is not affected by the response surface approach because the behavior of the NPSS engine cycle model can be fitted very accurately by simple algebraic equations as will be shown later.

Engine parameters required for the present flow simulations are a mass flow rate $\dot{m}$, total pressure P_t, total temperature T_t at the nozzle exit of each flow passage. Input variables to the NPSS model are total pressure recoveries η at fan faces. Since the corrected mass flow rate includes the recovery value at each fan face, it is the same and constant for the three passages with the amount of 259.22 *lb/s* at the full power TOC condition. Therefore, only P_t and T_t need to be defined by the response surfaces. There are three input variables; η_1, η_2, η_3, for passages 1 (center passage), 2 and 3 (two side passages), respectively. If all the variables are independent and coupled together, we need six functions, each of which is a function of the three input variables η_1, η_2, η_3:

$$
\begin{aligned}
P_{t\_exit1} &= f_{P1}(\eta_1,\eta_2,\eta_3),\ T_{t\_exit1} = f_{T1}(\eta_1,\eta_2,\eta_3) \\
P_{t\_exit2} &= f_{P2}(\eta_1,\eta_2,\eta_3),\ T_{t\_exit2} = f_{T2}(\eta_1,\eta_2,\eta_3) \\
P_{t\_exit3} &= f_{P3}(\eta_1,\eta_2,\eta_3),\ T_{t\_exit3} = f_{T3}(\eta_1,\eta_2,\eta_3)
\end{aligned}
\tag{1}
$$

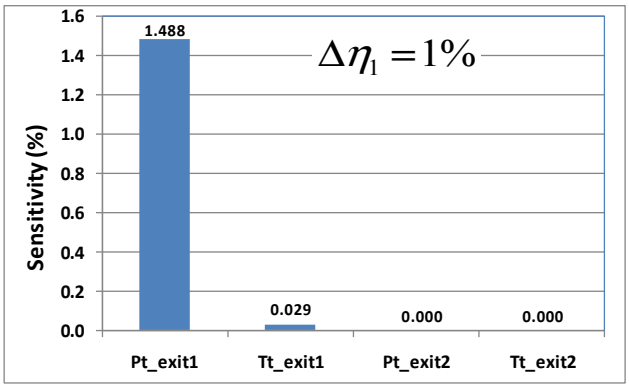

(a) When η_1 is varied by 1% point.

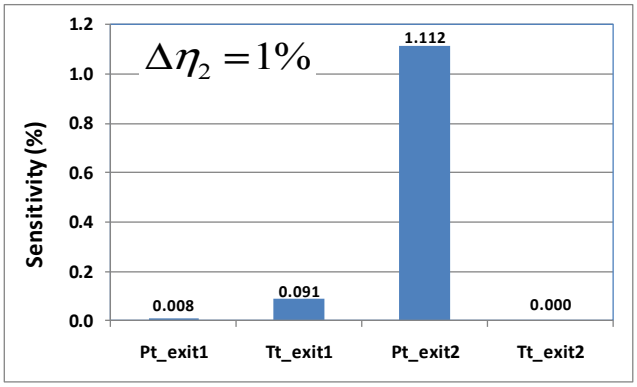

(b) When η_2 is varied by 1% point.

Fig. 5 Sensitivity of engine parameters with respect to changes in recovery at fan faces.

Sensitivities of engine parameters are calculated by finite differencing of off-design NPSS simulation results at the TOC condition for one percent point variation of the recovery at a fan face. Figure 5 shows some results of the sensitivity study. All other sensitivity terms not shown in Fig.5 are all zero. The results of the sensitivity study can be summarized as follows:

1) P_{t_exit} is affected significantly by the recovery of its own passage only.
2) T_{t_exit} of the central passage is affected by the recovery of the central passage, but the amount of sensitivity is negligible.
3) P_{t_exit}, and T_{t_exit} of the central passage are slightly affected by recoveries of side passages because the turbine work of the core engine to drive side fans is affected by recoveries at the side fan faces. However, the amount of sensitivity is negligible.
4) The recovery of the central passage has no effects on P_{t_exit} or T_{t_exit} of side passages.

Through the sensitivity study, the number of response surface models can be reduced from six to two; $f_{P1}, f_{P2,3}$, and each model is a function of only the recovery of its own passage.

$$\begin{aligned} P_{t\_exit1} &= f_{P1}(\eta_1),\ T_{t\_exit1} = const_1 \\ P_{t\_exit2} &= f_{P2,3}(\eta_2),\ T_{t\_exit2} = const_{2,3} \\ P_{t\_exit3} &= f_{P2,3}(\eta_3),\ T_{t\_exit3} = const_{2,3}, \end{aligned} \tag{2}$$

where T_{t_exit1} and $T_{t\_exit2,3}$ are set as 701 and 503°R, respectively according to NPSS results.

Data points for response surface models can be generated by conducting off-design simulations of the NPSS engine model at TOC for different inlet recovery values. In Fig.6, the resulting engine parameters of interest for engine exhaust plane boundary conditions are plotted, and least squares curve fitting is applied to obtain algebraic response surface models.

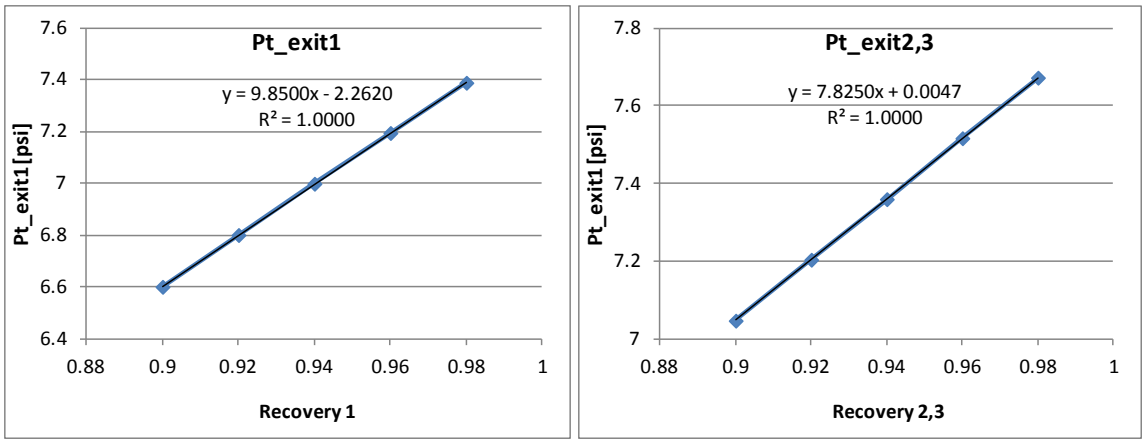

Fig. 6 Response surfaces for the NPSS engine model at the TOC maximum power condition with Mach 0.8, h=35 k ft.

III. Methodologies

A. Flow Solver

GO-*flow* [13], a finite-volume unstructured-grid Navier-Stokes solver, is used in the current flow simulations. The compressible Reynolds-averaged Navier-Stokes (RANS) equations are discretized by the cell-vertex finite volume method. Control volumes are non-overlapping dual cells constructed around each node. Each edge connecting two nodes is associated with an area vector of the control surface, at which flow fluxes are computed. For a second order accuracy, a linear reconstruction of the primitive gas dynamic variables inside the control volume is used in conjunction with a limiter. The inviscid flux is computed using approximate Riemann solvers. Turbulence effects are considered by using Menter's two equations Shear Stress Transport (SST) model [14, 15]. For the time integration, the Lower-Upper Symmetric Gauss Seidel (LU-SGS) implicit method is adopted [16]. Parallel processing is made by domain decomposition of the computational mesh and Message-Passing Interface (MPI). A validation study of the flow solver on a BLI offset inlet is presented in Appendix.

B. Computational Mesh Generation

Mesh generation is conducted using MEGG3D (Mixed Element Grid Generation in 3D) code [17, 18]. A triangular surface mesh is generated directly on Stereolithography (STL) data, which can be exported from a CAD model. A hybrid volume mesh is then made by using advancing front/layer methods. Prism layers are generated near viscous walls, tetrahedral cells in the remaining computational domain and pyramid cells in between when necessary. Figure 7 (a) displays a surface mesh for the N2B model. Figure 7 (b) shows a top view of duct system splitting into three branches. The surface mesh near nozzles is shown in Fig.7 (c). As mentioned earlier for Fig.2 (b), the N2B aircraft has variable area thrust vectoring nozzles, which inevitably contain moving parts contacting each other or having very small gaps in between. The complex geometry of the movable devices was simplified into clean exhaust nozzles as shown in Fig.7 (c). If the thrust vectoring function needs to be simulated, the simplified surface geometry can be deformed for that purpose.

The total number of computational mesh points for the half model of the N2B configuration is about 13.3 million, and first nodes off the viscous walls are clustered to the wall so that y+ values at the first nodes are less than 2.

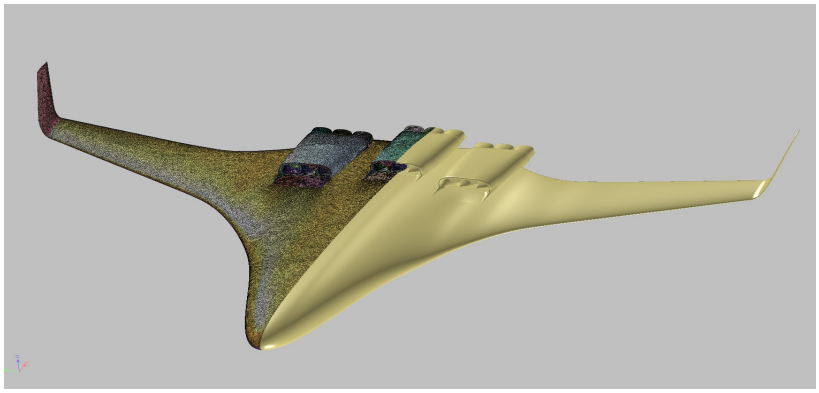

(a) Surface mesh for symmetric half model.

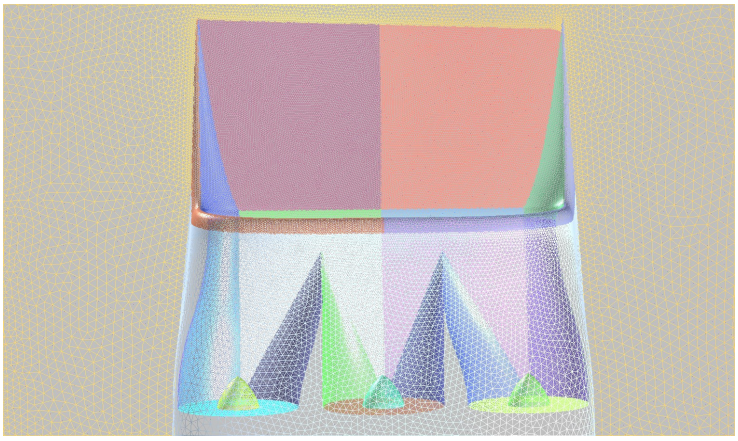

(b) Top view of S-duct and spinners at fan faces

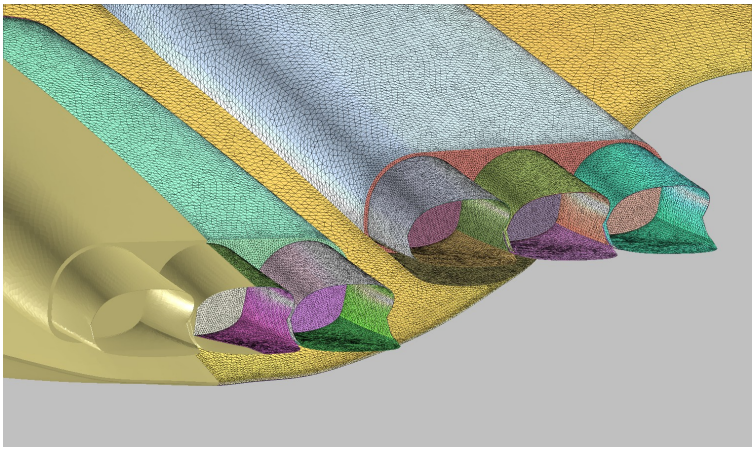

(c) Near the nozzles

Fig. 7 Surface mesh for the N2B configuration

C. Boundary Conditions

Freestream conditions are the TOC flight conditions at Mach number of 0.8 and altitude of 35,000 ft presented in Table 2. For the engine fan face boundary conditions, we extrapolate the density and velocity components from inside of computational domain and impose a uniform static back pressure to match the target mass flow rate.

The conventional uniform back pressure boundary condition for fan faces has been widely used for inlet-engine interaction problems [9, 19, 20]. For propulsion-airframe integration problems with highly distorted onset flows at fan

faces, the assumption of uniformity of fan face static pressure may not be valid any more. At a low recovery region on an AIP, the low momentum causes larger local incidence angle for the fan blade section leading to a stronger suction effect by the fan, which mitigates the flow distortion. Therefore, the use of the uniform back pressure boundary condition is known to give conservative results in terms of the flow distortion at fan faces.

A direct coupling of the inlet and full annulus fan blades in the computational domain would give a more realistic inlet fan interaction simulations, but it would require prohibitively large computational cost for shape design applications. As an alternative to the coupling with a full annulus fan blades simulation, the body force approach [21, 22] has been drawing attentions, The body force approach models rotor/stator blade row turning, loss and deviations using body force terms, which are integrated for a control volume around each blade row. The body force approach still requires more computational cost than the current uniform static back pressure approach due to the pre-analyses of single blade passages for body force model generation and increment of the mesh size as computational domains between fan faces and exhaust planes are included. However, application of the body force approach for more accurate inlet fan interaction would be beneficial especially for BLI inlet diffuser flows. The uniform back pressure approach adopted in the present study paper is still valid for qualitative comparisons on inlet fan interaction problems when diffuser flow separation does not reach to the fan face [22]. More realistic simulation of the inlet fan interaction effects remains for future work.

For the engine nozzle exhaust planes, the total pressure and total temperature are set and a static pressure is taken from downstream in the computational domain for subsonic inflow boundary conditions.

D. Distortion indicators

Flow distortion at fan faces can be quantified by calculating flow distortion indicators. In this study, two circumferential distortion indicators are selected and calculated; one indicator is $DPCP_{avg}$, and the other one is DC60.

$DPCP_{avg}$ is the average SAE circumferential distortion indicator defined in the Aerospace Recommendation Practice (ARP) 1420 standard [23].

$$DPCP_{avg} = \frac{1}{N_{rings}} \sum_{i=1}^{N_{rings}} Intensity_i \,, \tag{3}$$

where i is the ring number on the AIP rake and N_{rings} is the total number of rings. The distortion intensity for ring i is defined as

$$Intensity_i = \frac{PAV_i - PAVLOW_i}{PAV_i}, \tag{4}$$

where PAV_i is the area-weighted average total pressure of ring i and $PAVLOW_i$ is the area-weighted average of the total pressure lower than PAV_i.

DC60 [24] is defined as

$$DC60 = \frac{P_{Tavg} - P_{T60}}{q_{avg}}, \tag{5}$$

where P_{Tavg} is the mean total pressure at the AIP, P_{T60} is the mean total pressure on the worst 60° sector having the lowest mean recovery, and q_{avg} is the mean dynamic pressure calculated by

$$q_{avg} = P_{Tavg} - P_{avg} \,, \tag{6}$$

where P_{avg} is the area-weighted average static pressure at the AIP.

Computational results are interpolated onto 120 probe locations at an AIP, which are obtained by rotating a 40-probe total pressure rake by 0, 15 and 30 degrees. The 40-probe rake follows the SAE standard [23] and has eight arms with five total pressure probes on each arm in the radial direction.

E. Sensitivity Analysis

Sensitivity analysis is one of the most important components to a gradient-based design optimization. The adjoint methods [25-29] allow efficient calculation of objective function gradients for a computational cost independent of the number of design variables. In the present study, we adopt a discrete unstructured Navier-Strokes adjoint solver

[28, 29] developed from the flow solver described above in Section 3.A. The adjoint solver uses GMRES [30] for the time integration with LU-SGS as a preconditioner. Parallel processing is also made by domain decomposition of the computational mesh and Message-Passing Interface (MPI).

F. Geometry Parameterization

NURBS (Non-Uniform Rational B-Spline) [31] is an industry standard for free form shape representation in CAD. With k^{th} order surface representation, C^{k-2} continuity is guaranteed. A NURBS surface is represented by basis functions and control points as

$$\begin{aligned} \boldsymbol{P}(u,v) &= \big(x(u,v), y(u,v), z(u,v)\big) \\ &= \frac{\sum_{i=0}^{m}\sum_{j=0}^{n} N_{i,k}(u) N_{j,l}(v) \omega_{i,j} \boldsymbol{Q}_{i,j}}{\sum_{i=0}^{m}\sum_{j=0}^{n} N_{i,k}(u) N_{j,l}(v) \omega_{i,j}}, \end{aligned} \tag{7}$$

where u and v are parametric coordinates, $\boldsymbol{Q}_{i,j}$ is the coordinate vector of a control point, $N_{i,k}$ and $N_{j,l}$ are blended basis functions of orders k and l in the u and v directions, respectively, and $\omega_{i,j}$ is the weight of the control points. $(m+1)$ and $(n+1)$ are numbers of control points in u and v directions, respectively. In the present study, $\omega_{i,j}$ is treated as a constant and set as 1.0 for equal weights for control points, and $k=l=4$ for a 4th order surface representation.

The basis function N is defined as follows:

$$N_{i,k}(u) = \frac{(u-t_i) N_{i,k-1}(u)}{t_{i+k-1}-t_i} + \frac{(t_{i+k}-u) N_{i+1,k-1}(u)}{t_{i+k}-t_{i+1}}, \tag{8}$$

$$N_{i,1}(u) = \begin{cases} 1 & t_i \le u \le t_{i+1} \\ 0 & otherwise \end{cases}, \tag{9}$$

where t_i are knot values, that are clustered in the v coordinate to the cowl lip for the cowl design surfaces in Fig.8 (a), and evenly distributed for diffuser surfaces in Fig.8 (b). In the u coordinate, the knot values are evenly distributed for all design surfaces.

Design surfaces in the three-dimensional physical space are transformed into a two-dimensional parametric rectangular u-v space. The fixed boundary parameterization is conducted with a spring model in which each edge of the surface mesh is replaced with a tension spring, spring coefficients of which is inversely proportional to the edge length. Then minimization of the total energy of springs for the design surfaces with proper boundary conditions for u and v at each mesh nodes results in smoothly distributed design surface nodes in u-v space as shown in Fig.8.

The design surface in u-v space is perturbed in the normal direction by moving control points of NURBS. The shape modification is then transformed back to the physical space. Figure 8 (a) shows design surface parameterization for cowl surfaces. The number of design parameters for the two cowl surfaces is 80. In Fig.8 (b), parameterization of design surfaces for bottom and side walls of diffusers are illustrated. Vertical struts dividing flow passages for three fans are not designed. However, as the bottom surface is modified, the struts are deformed accordingly. The number of design parameters for the diffuser surfaces is also set as 80.

For the cowl lip shape modification, the nacelle surfaces are deformed by a spring analogy and constrained to be sliding along the upper wing surface. All the surface mesh patches under deformation are divided into two groups; primary and secondary deforming patches. The primary surface patches include cowl surfaces and upper, bottom and side walls of the diffuser surfaces. The primary patches are directly deformed by a spring analogy with the cowl lip deformation as boundary conditions. Once the primary patches are deformed, the spring analogy is applied to the secondary patches such as diffuser struts and the wing upper surface according to the deformation of the primary patches. The geometry of strut surfaces are deformed with the new primary patch shapes as boundary conditions. On the other hand, the wing upper surface geometry is not altered, and the upper wing surface mesh points are moved along the curved surface. This two-step deformation allows more smooth geometry modification especially around the surface junctions. Figure 9 shows an example of cowl lip shape modification. Height and width of the cowl lip shape are used as design parameters, therefore, 4 design parameters (two for each inlet) are added to the design variable set. The total number of design parameters is 164 (80 for cowl surfaces, 80 for diffuser surfaces and 4 for cowl lips).

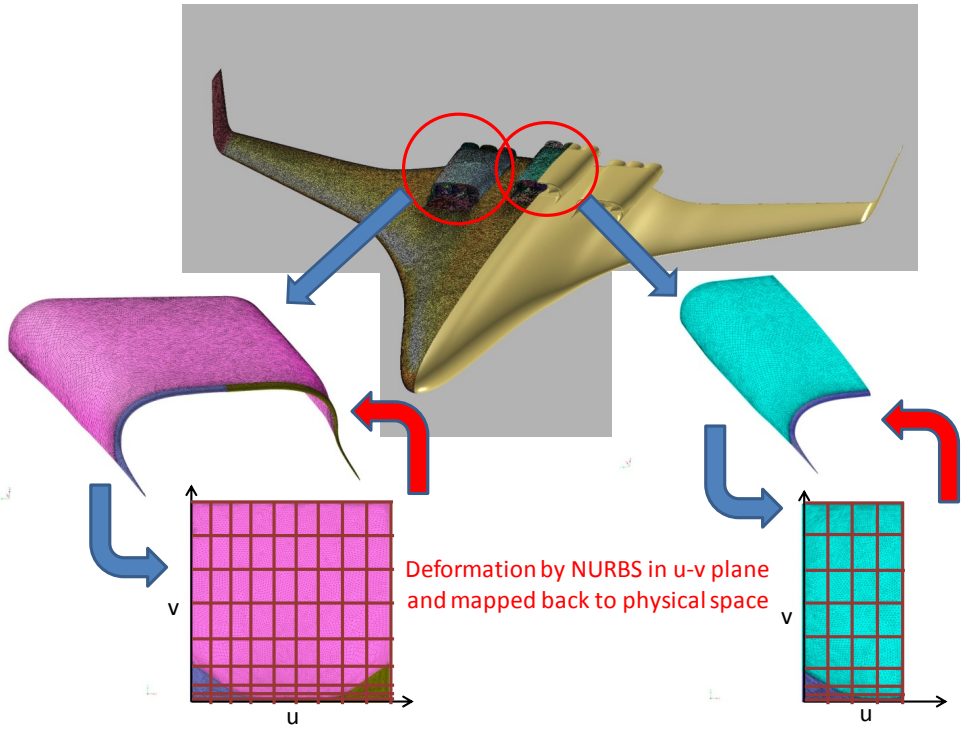

(a) Parameterization of cowl surfaces

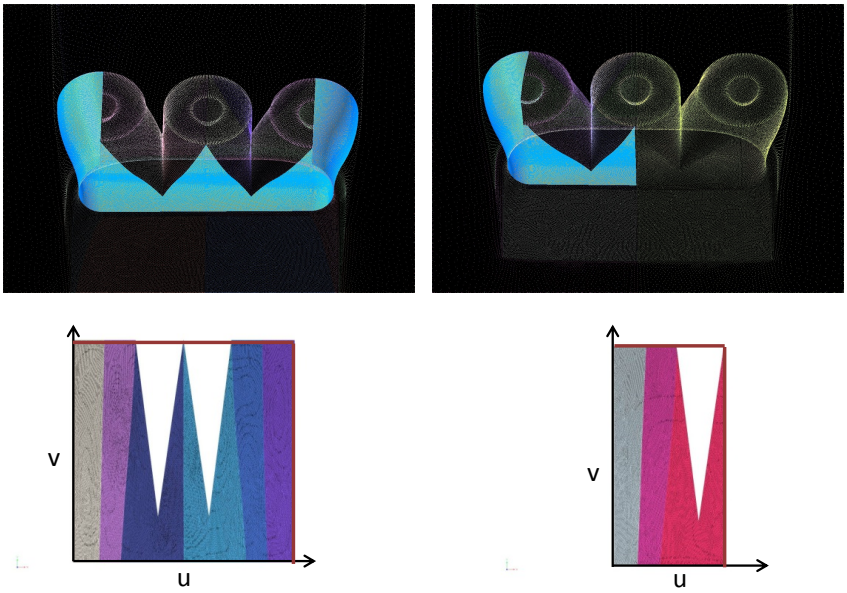

(b) Parameterization of diffuser bottom and side surfaces

Fig .8 u-v Parameterization of design surfaces

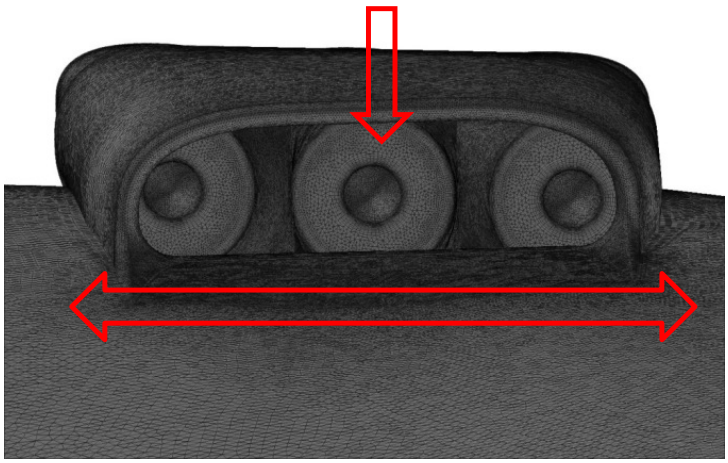

(a) Initial

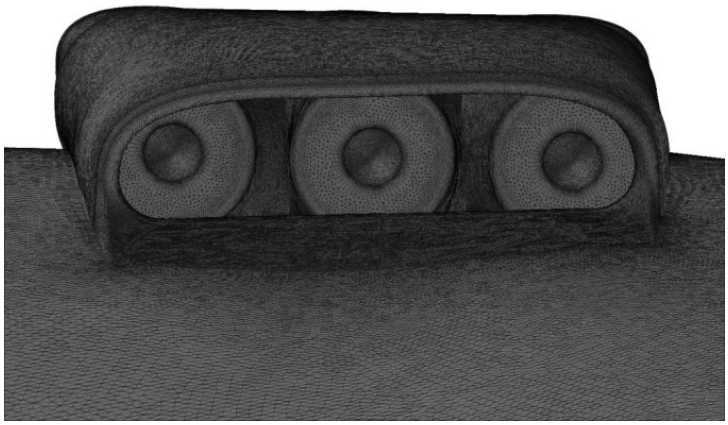

(b) Modified

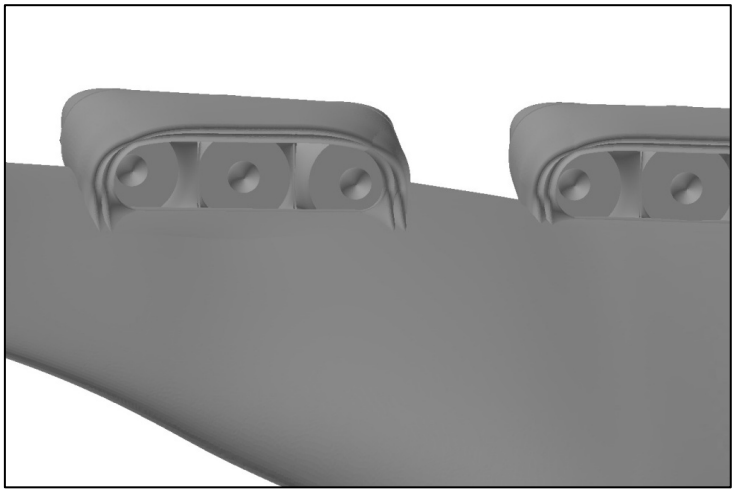

(c) Overlapped view

Fig .9 An example of cowl lip shape deformation by a spring analogy approach

When the surface mesh is perturbed by the design parameterization methods, volume mesh points are also moved accordingly by a spring analogy with a spring coefficient inversely proportional to the edge length. The required computational cost for the grid modification is negligible compared to the computational cost of flow simulations.

G. Overall Design Procedure

The overall design procedure is shown in Fig.10. First, a flow analysis is conducted for the current design configuration. Then an adjoint sensitivity analysis is performed based on the flow analysis results to determine a search direction. A step size along the search direction is selected by a line search method with the slope along the search direction. In the present study, a quadratic polynomial fitting is used for the line search. Then design variables are updated using the gradient information and step size. Design surfaces are then modified using the aforementioned design parameterization, and volume meshes are modified accordingly using the spring analogy. This loop is repeated until the design converges. As a gradient based optimizer for the unconstrained minimization problem, the conjugate gradient method [32] is employed.

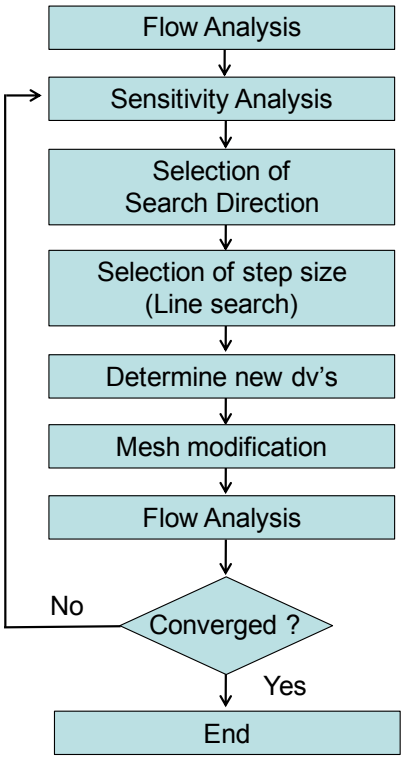

Fig. 10. Overall shape design procedure

IV. Flow Simulation Results

The integrated airframe-nacelle configuration shows complex flow features. Figure 11 (a) shows envelops of separation bubbles with negative u velocity component. Many separation bubbles are present around the nacelle;.inside of inlet diffusers, on the cowl surfaces, and nacelle base regions. In all the color contours in this paper, the static and total pressure values are normalized by the freestream static and total pressures, respectively.

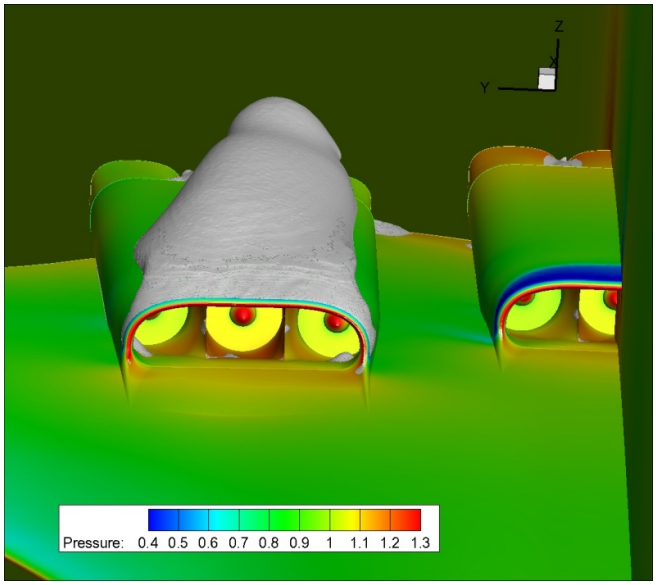

(a) Separation bubble envelops around the BLI inlet nacelle

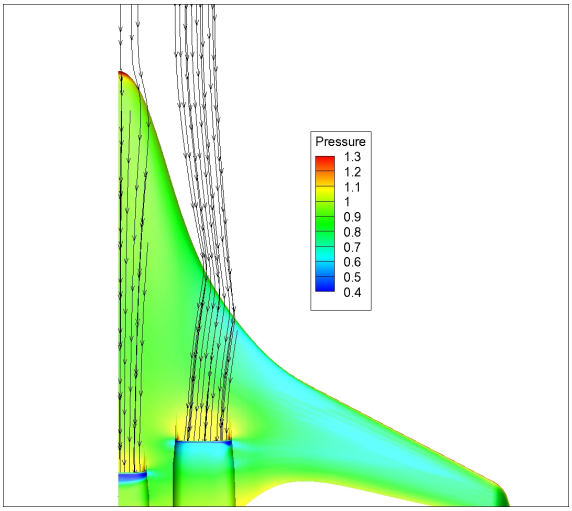

(b) Streamlines into the engine faces. Color contours represent the normalized static pressure.

Fig. 11. Streamlines into the engine faces. Color contours represent the normalized static pressure.

Streamlines into the engine faces are visualized in Fig.11 (b), which shows local yaw angle of the onset flow to the outboard inlet. This yaw angle of the local flow is consistent with the Ref.[34] and explains the shape of the separation bubble trailing with a yaw angle on the cowl surface of the outboard inlet in Fig.11 (a).

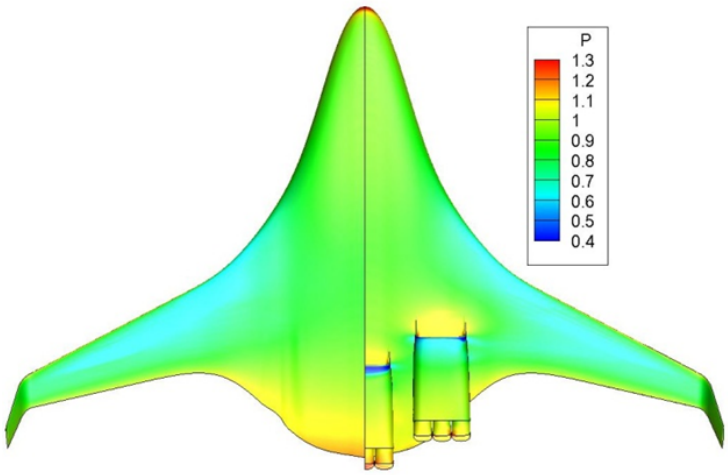

Fig. 12. Comparison of upper surface pressure contours of N2B and clean wing HWB at Mach 0.8, altitude 35,000 ft., and AOA 3.5deg. (left: clean wing, right: N2B).

The upper surface pressure contours for the N2B and clean wing HWB which does not have any engine installed are compared in Fig.12. The installation of embedded engine nacelles on the upper surface causes higher pressure in front of the inlets due to the pre-compression. The lift coefficients of the clean HWB and N2B are 0.237 and 0.167, respectively at the flow condition. In Ref. [34] C_L of BLI configurations at a constant angle of attack increased compared to a strut-mounted configuration because the precompression is more than compensated by the accelerated low pressure flow region on the cowl surface. In the N2B case this compensation does not happen or is too weak, and one of possible reasons is the massive flow separation on the outer inlet cowl.

Distributions of pressure coefficients at selected wing sections are displayed in Fig.13. The y=0.01 section shows N2B has an accelerated flow terminated with a strong shock wave on the cowl surface. The higher pressure infront of the inlet entrance is also evident in Fig.13 (a) and Fig.13 (c). Higher pressure on the upper wing surface is propagated to outboard sections such as y=0.3 and y=0.5 (Fig.13(d) and (e)).

The ingested boundary layer can be visualized by total pressure contours at the center section of each inlet, as shown in Fig.14. The center inlet has a thicker boundary layer ingested into the diffuser than the side inlet, because of the longer distance form the airframe leading edge to the inlet entrance. Mach contours in Fig.14 also show flow separation patterns on the upper surface of the nacelle. It is noted that there is a big difference in surface slopes in front of the offset inlet at the symmetric plane and the center plane of the outer inlet. At the symmetry plane, the upper wing surface before entering the inlet is relatively well aligned with the cowl surface. On the other hand, at the center plane of the outer inlet, the cowl angle has a quite large relative incidence angle to the incoming flow along the upper surface. This relative angle of attack of the cowl lip is causing a leading edge separation on the cowl surface of the outer inlet. This is due to the fact that the x/c (relative longitudinal location to the section airfoil chord length) of the inlet entrance is abount 77% for the symmetric plane and 61% for the center plane of the outer inlet. The difference of local x/c means a difference in local slopes of the sectional airfoil surfaces. Since a HWB aircraft tends to have a large spanwise variation in the section chord length, cowl lip angles of embedded engine nacelles should be designed to align with local inflow directions.

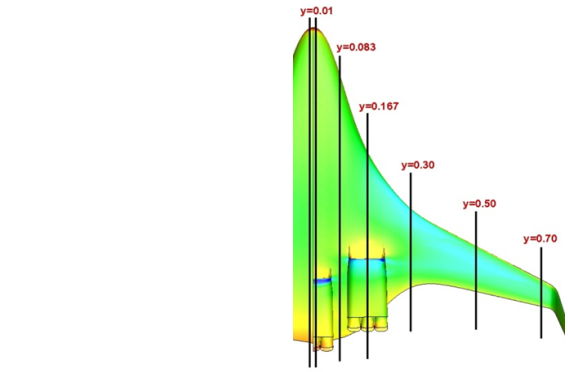

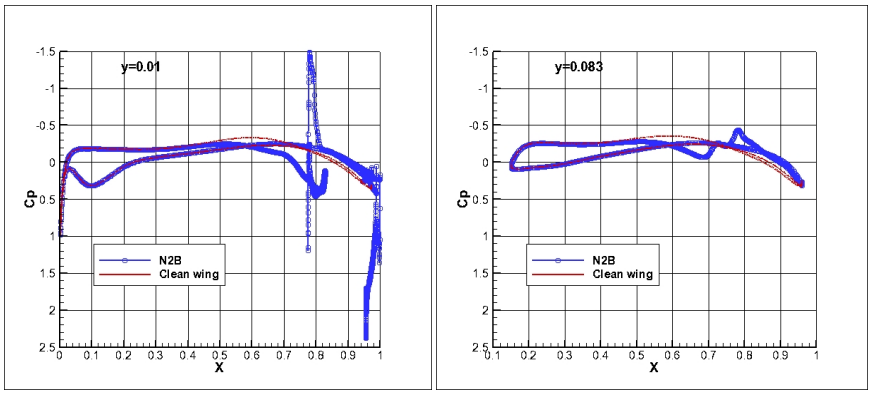

(a) y=0.01 (b) y=0.083

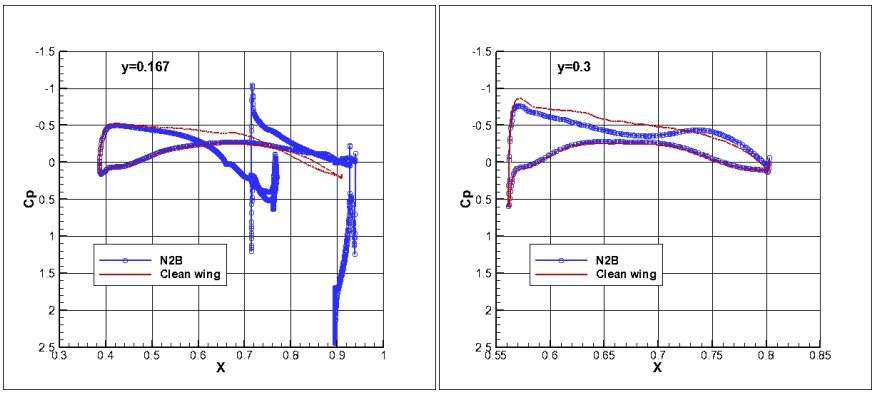

(c) y=0.167 (d) y=0.300

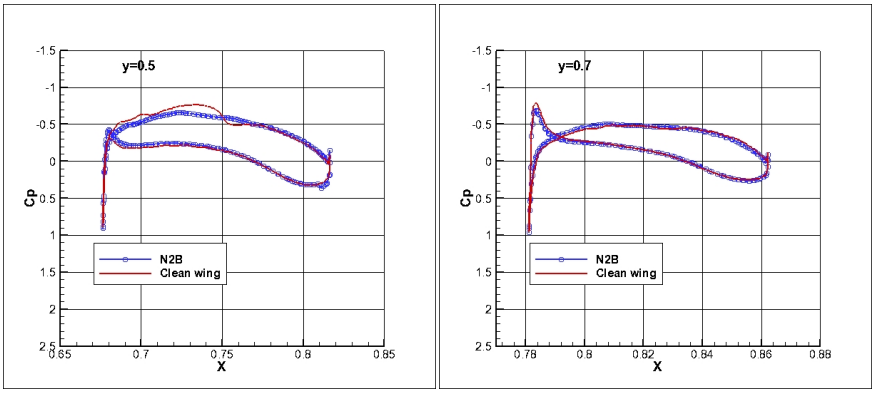

(e) y=0.500 (f) y=0.700

Fig. 13 Comparison of section pressure distributions between clean wing and N2B at Mach 0.8, altitude 35,000 ft., and AOA 3.5deg.

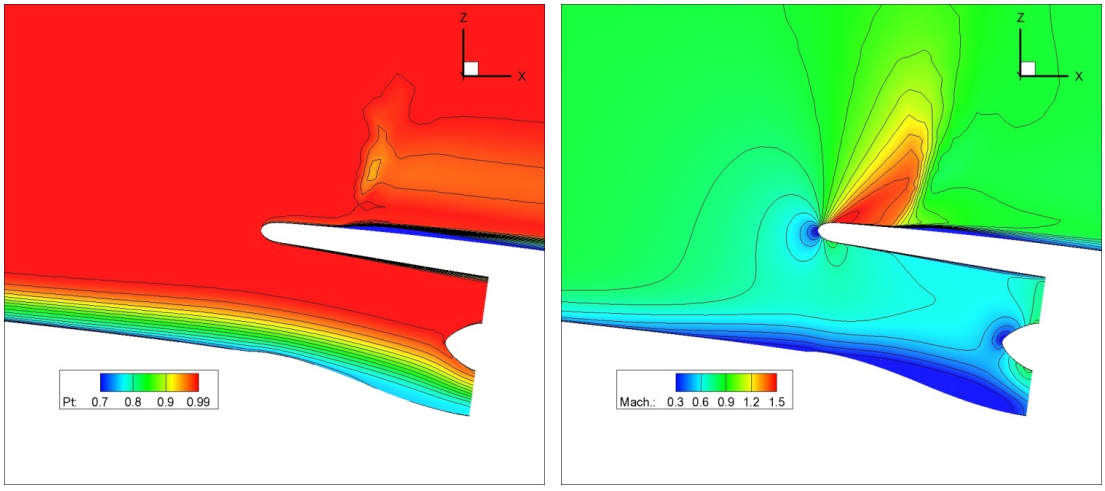

(a) Normalized total pressure and Mach contours at symmetric plane.

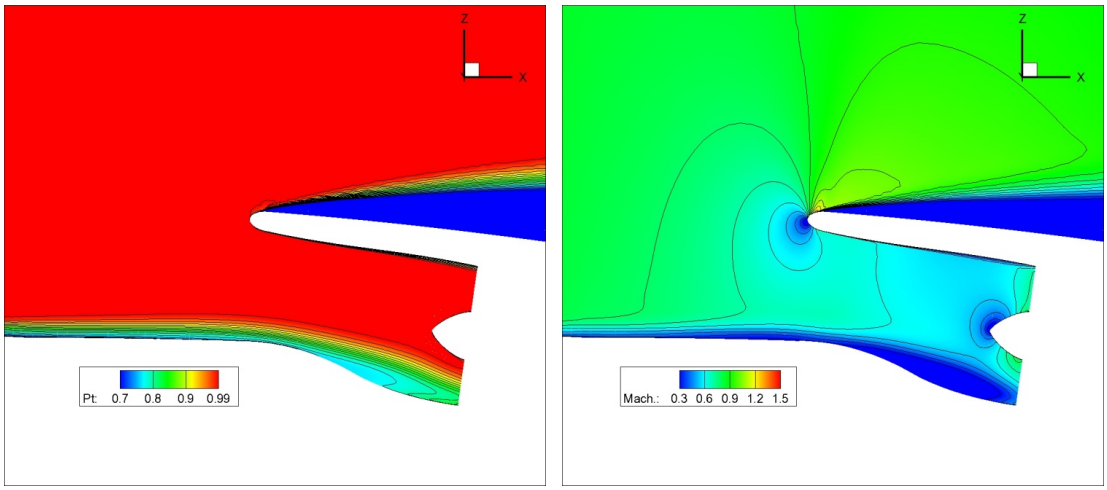

(b) Normalized total pressure and Mach contours at the center plane of outboard inlet

Fig. 14. Total pressure and Mach contours at inlet center sections

The boundary layer edge lines of the N2B and clean wing configurations are compared in Fig.15. The boundary layer edge lines in the figure is defined as the contour line of 99% total pressure relative to the freestream total pressure. Boundary layer profiles obtained from CFD simulations of a clean wing configuration has been widely used for the sizing of the inlet capture area for BLI offset inlets and estimation of pressure recovery at fan faces of embedded engines [16, 3]. As can be seen in Fig.15, boundary layers have very similar thicknesses between the two configurations on the upper surface far upstream from the inlet entrance and the lower surface. However, as the flow on the upper surface of N2B approaches to the inlet, the boundary layer thickness gets thicker than that of the clean wing because of the adverse pressure gradient due to the pre-compression in front of the inlet. Some quantitative comparisons of the BL thicknesses are made in Table 3 , which shows that the N2B has thicker boundary layers than the clean wing at inlet throat locations and the thickness increment gets larger for thicker bounday layers.

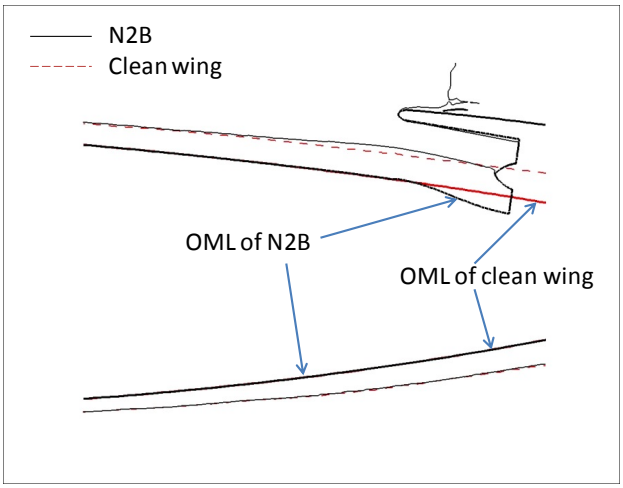

(a) Symmetric plane

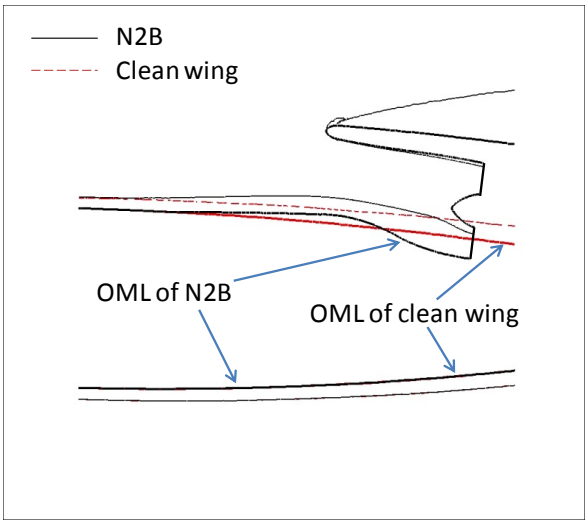

(b) Center plane of outboard inlet

Fig. 15 Comparison of boundary layer edge lines for N2B and clean wing configurations

Table 3 Boundary layer thickness at inlet throat relative to inlet throat height

Section	Cleanwing	N2B	Increment (%)
Symmetric plane	0.43	0.52	21
Center plane of outer inlet	0.19	0.21	11

Total pressure contours in the inlet diffusers along the x coordinate are shown in Fig.16, which clearly shows the difference in the thickness of ingested boundary layers between the side and center inlet. Also, it can be noted that at the entrance of the side inlet (x = 0.718), the boundary layer thickness decreases in the spanwise direction. The minimum recovery occurs at the corner between bottom and side walls in the diffuser.

In Fig.17, compared are recoveries of the side inlet obtained by clean wing simulation results and the present N2B analysis result. In Fig.17, AIP1 is the left-most fan face in the front view, and AIP5 is the center fan face as depicted in the bottom of Fig.16. As mentioned earlier in Section II-B, the recoveries estimated in Ref. [3] are based on clean wing analyses and used as input values to conceptual design of the engine. The single valued recovery at the central passage (AIP3) for the estimation based on clean wing results were obtained by mass-weighted averaging of the bypass and core recoveries with the design BPR 3.1. The recoveries by the estimation based on the clean wing results and present N2B analysis results are in good agreement. For AIP2, the recovery values match more closely, and for AIP1 and AIP3 the present calculation shows lower recovery than the clean wing result. Clean wing results for

recoveries of the center inlet are not available in Ref.[3]. For the present N2B simulations, the recoveries for the center inlet (AIP4 and AIP5) are about a couple of percents lower than the side inlet recoveries as shown in Fig. 17 due to the thicker boundary layer for the center engine inlet.

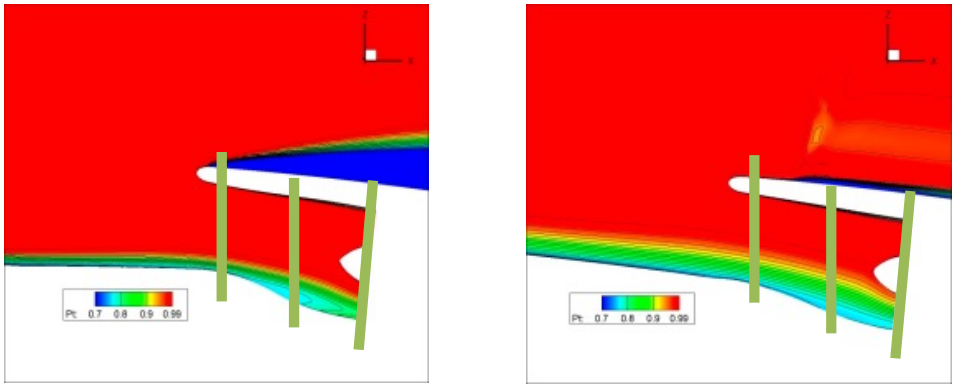

(a) Locations of streamwise section cuts

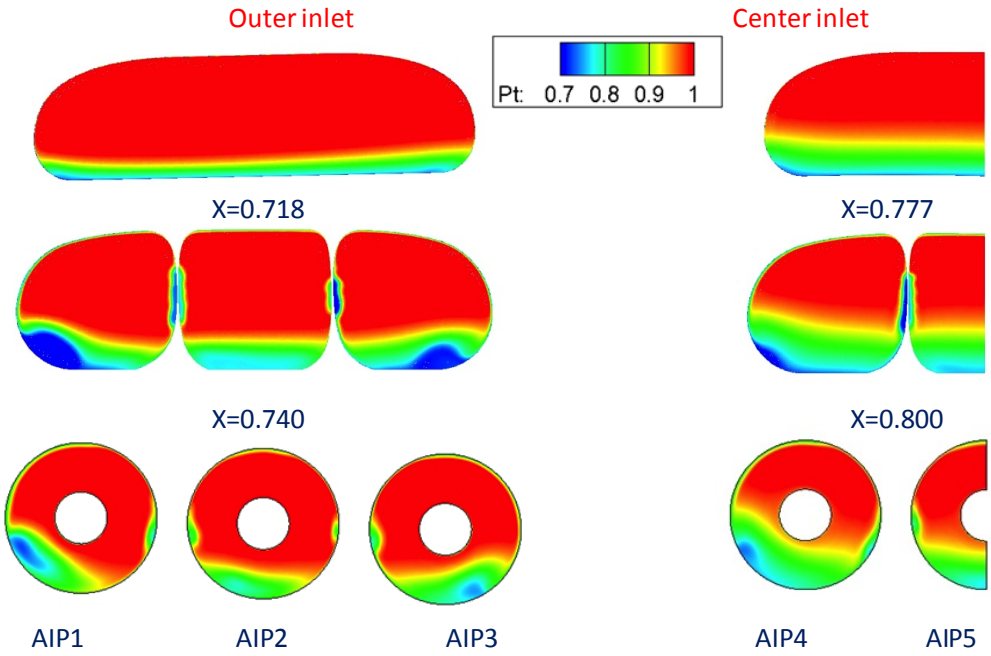

Fig.16 Normalized total pressure contours inside diffusers for initial N2B configuration

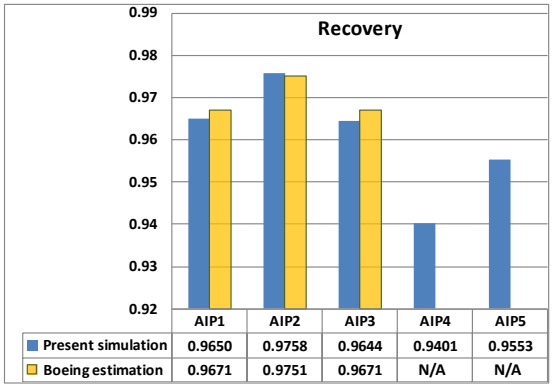

Fig.17 Total pressure recovery at AIPs (fan faces).
AIP1 is the outmost fan face, and AIP5 is the center fan face.

The calculated distortion indicators for the five fan faces are presented in Fig.18. It is noted that $DPCP_{avg}$ and DC60 have the smallest value at AIP2 because of thinner onset boundary layer and lack of side wall effects. Also, AIP4 has much larger $DPCP_{avg}$ value than AIP5 due to the side wall boundary layer. DC60 has a different trend for AIP4 and AIP5 from the $DPCP_{avg}$.

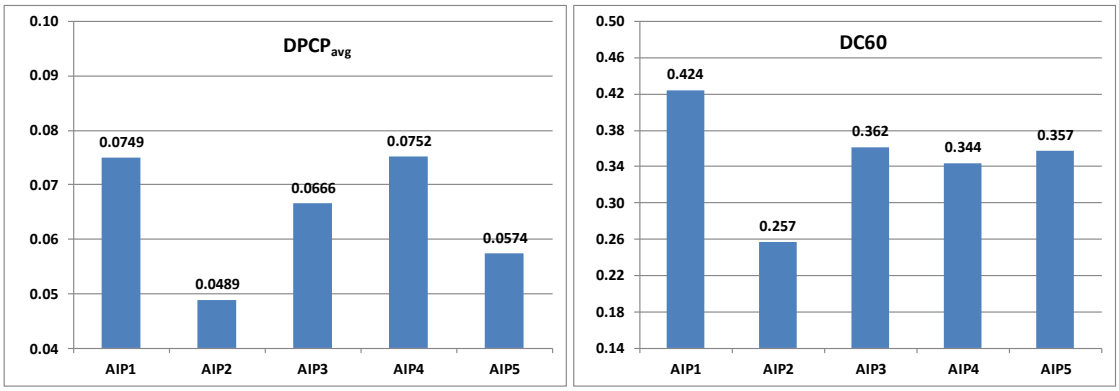

Fig. 18 Distortion indicator values at AIPs

In Fig.19, local Mach number contours at the symmetric plane are shown around the nozzle flow, which is choked at the throat. Under the nozzle a separation zone exists with very low local Mach number. The separated base region would significantly increase the drag force. More compactly integrated installation of the engine nacelle is thus needed reducing the area of the base region for better aerodynamic performance of the HWB. Separation bubbles in the base region will also be depicted later in Fig. 20.

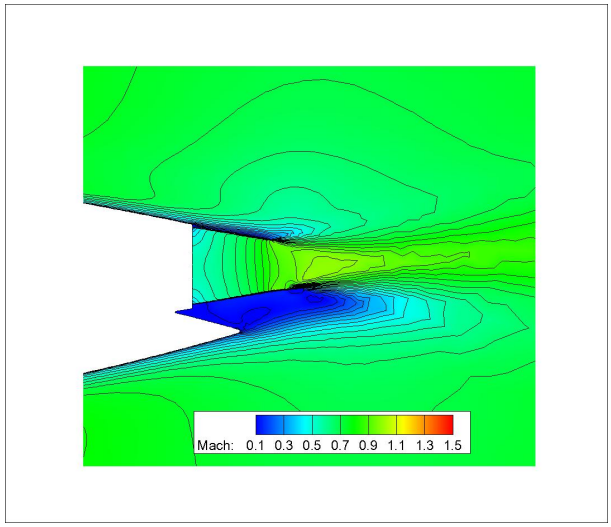

Fig. 19. Mach contours near nozzle exhaust at the symmetric plane

V. Optimal Inlet Shape Design

The optimal shape design is conducted in two separate steps; the first step is a drag minimization to improve flow characteristics of the integrated airframe-nacelle by reducing flow separations and shock wave strengths. The second step is a distortion minimization taking the result of the first step as a starting point. Hereafter, the results of the drag minimization and distortion minimization will be referred to as Design 1 and Design2, respectively.

A. Design 1: drag minimization

The design objective is to minimize the drag coefficient at a fixed angle of attack. The drag coefficient is calculated by surface integration of pressure and skin friction forces on viscous surfaces. The thrust coefficient appearing later in Eq. (8) is calculated by surface integration of pressure forces and momentum fluxes on fan faces and engine exhaust planes.

The objective function is defined as follows:

$$F = C_D + \left.\frac{\partial C_D}{\partial C_L}\right|_{C_{L_0}} \left(C_{L_0} - C_L\right), \tag{6}$$

where the second term in the right-hand side is a penalty term that prevents the design from reducing the drag by simply reducing the lift force. The $\partial C_D/\partial C_L$ term can be calculated by a sensitivity analysis or a finite differencing for a perturbation of angle of attack. A simple alternative way is to use the quadratic relation between C_L and C_D as follows [35].

$$C_D = C_{D_0} + KC_L^2, \tag{7}$$

from which $\left.\frac{\partial C_D}{\partial C_L}\right|_{C_{L_0}} = 2KC_{L_0}$, where $K = \frac{1}{\pi AR}$.

The design optimization process to minimize the drag force may have impacts on the total pressure recovery at AIP, which affects the engine performance. The effects of recovery on the engine thrust force should be included in the objective function because reduction in thrust can be considered equivalent to increase of the drag. For this end the objective function is modified as follows:

$$F = C_D + \left.\frac{\partial C_D}{\partial C_L}\right|_{C_{L_0}} \left(C_{L_0} - C_L\right) + \sum_{i=1}^{N_{AIP}} \frac{\partial C_T}{\partial \eta_i}\left(\eta_{i_0} - \eta_i\right), \tag{8}$$

where N_{AIP} is the number of AIP on the configuration, η_i is the total pressure recovery at fan face *i*. C_T in Eq.(8) is engine thrust coefficient, which is nondimensionalized by the free stream dynamic pressure and reference area in the same way as the lift and drag coefficients. The $\partial C_T/\partial \eta_i$ terms are calculated using the NPSS engine model by a finite difference approximation. At the design flow condition with full powered engines, $\partial C_T/\partial \eta = 0.60\times10^{-2}$ for a central AIP and 0.39×10^{-2} for a side AIP of the tri-fan engine, which means one percent point change in recovery at an AIP results in roughly a half (0.39~0.60) count variation in thrust force.

The cowl surfaces and diffuser surfaces are designed with 164 parameters: 80 for outer cowl surfaces, 80 for diffuser surfaces and 4 for cowl lip shape deformation.

By Design 1, drag coefficient was reduced by 45 counts, and lift coefficient was increased from 0.167 to 0.193, which is still lower than the clean wing lift coefficient 0.237. Additional increment of the lift coefficient would be possible if the whole topology of the engine nacelle including the base region is changed in the shape design. Figure 20 compares separation bubbles of the initial and Design 1 configurations. Most separation bubbles are removed on the cowl surfaces by the design. And a new separation bubble appears on the right hand side of side nacelle of Design 1 due to local yaw angle of the incoming flow. Rear and side views of the separation bubbles in Fig.20 clearly show the change of separation bubble patterns before and after the design.

Local Mach number contours are compared for initial and design1 configuration in Fig. 21. The design shape has a larger cowl lip radius and thicker cowl than the initial shape. On the symmetric plane, flow is less accelerated along the cowl leading edge on the upper surface and shock strength got much weakened on the cowl. On the center plane of the side inlet, the separation bubble got removed and flow is more accelerated on the cowl surface as the local flow angle is more aligned by the cowl design. The cowl section shapes are directly compared in Fig. 22 for constant-y sections.

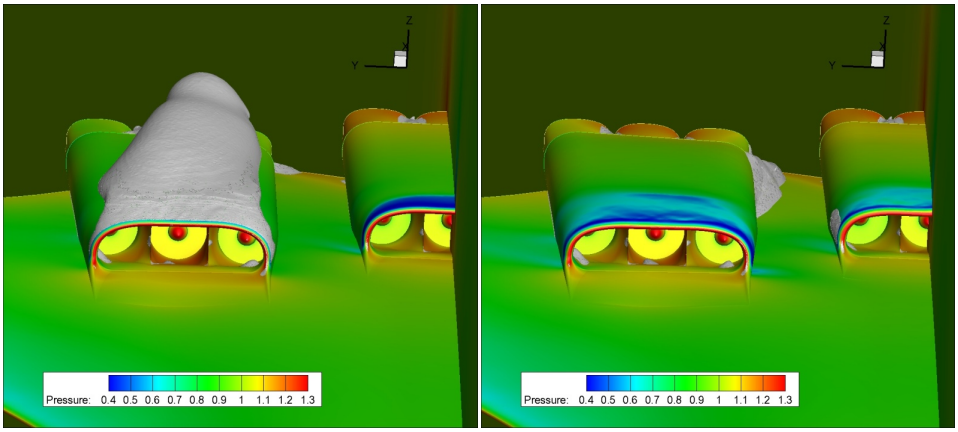

(a) Front view

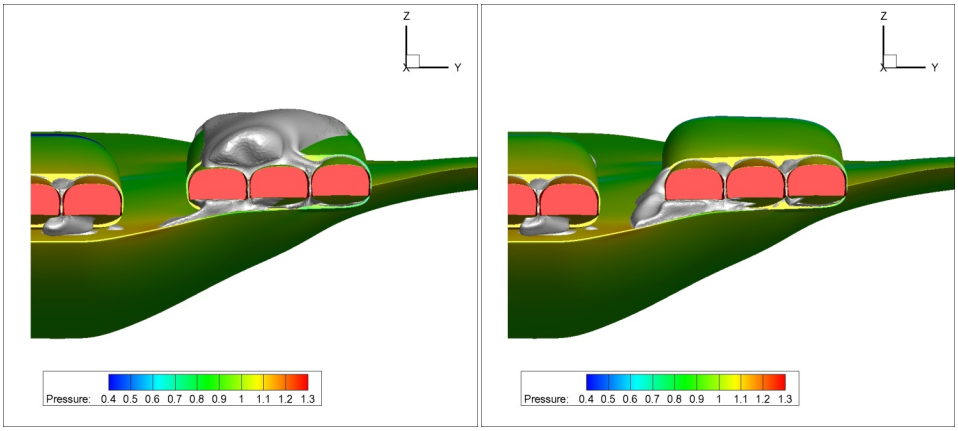

(b) Rear view

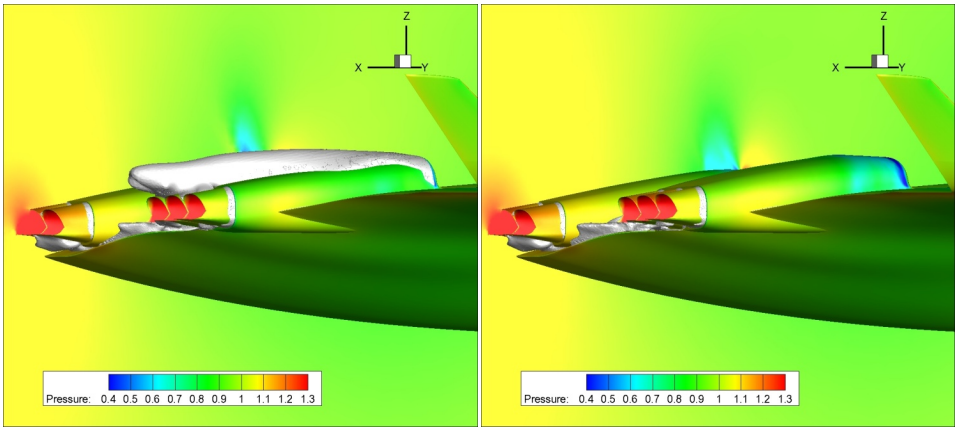

(c) Side view

Fig. 20 Separation bubble envelops for initial (left) and Design 1 (right) configurations

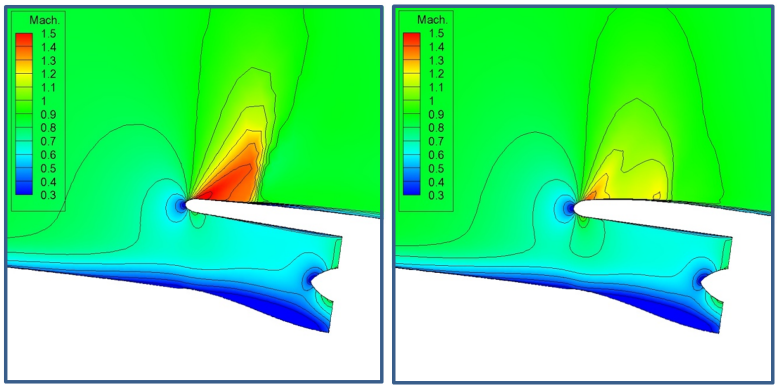

(a) Symmetric plane

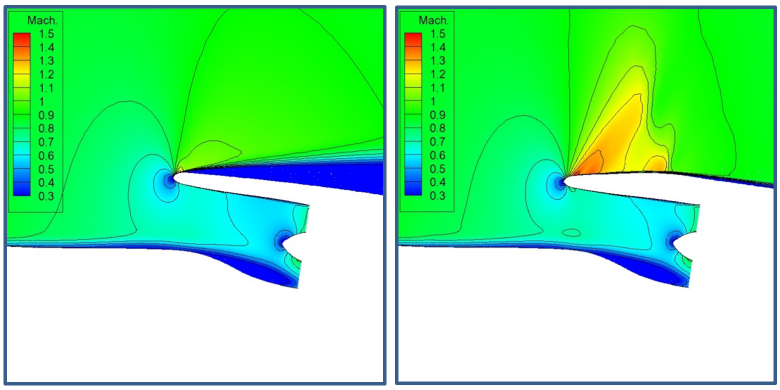

(b) Center plane of outer inlet

Fig. 21 Mach contours for initial (left) and design (right) configurations

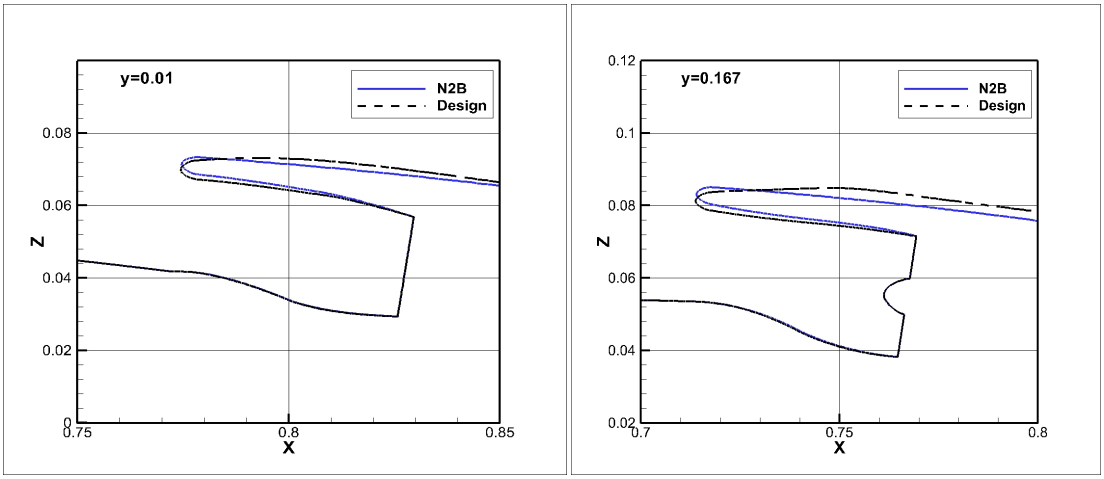

Fig. 22 Comparison of cowl shapes at constant y sections

Distributions of pressure coefficients at selected constant-y sections are shown in Fig. 23. The surface pressure distributions show all the flow features of the design configuration such as reduced shock strengths and lower overall pressure on the cowl surfaces. Also, the steeper and higher flow acceleration on the cowl lip lower surfaces presents the effects of increased cowl lip radius and decreased local flow incidence angles.

Total pressure contours of initial N2B and Design 1 at fan faces are compared in Fig.24, which appear almost similar to each other.

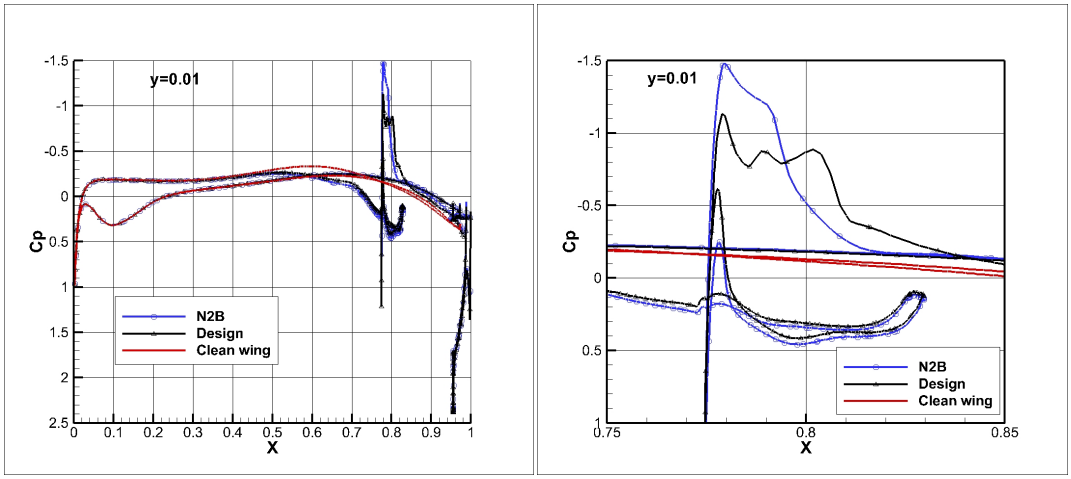

(a) y = 0.01

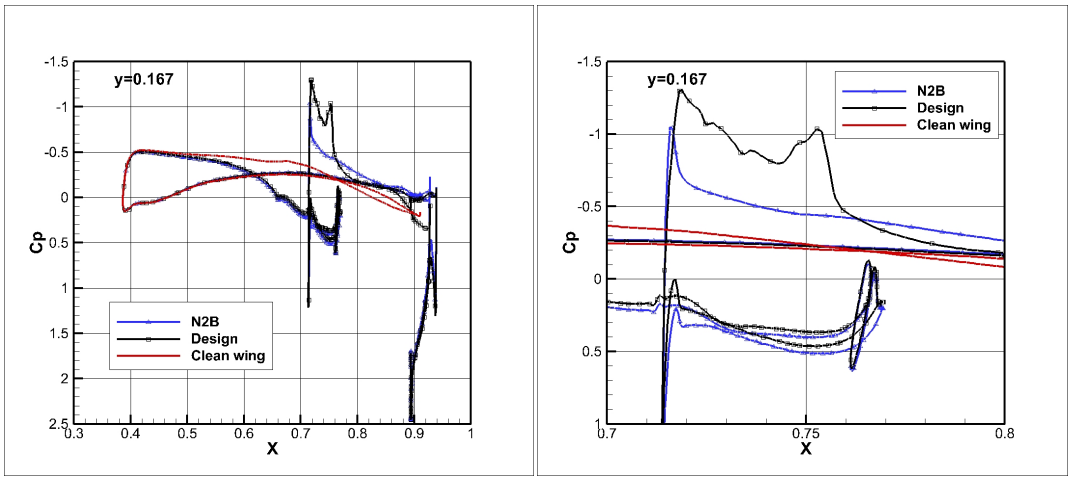

(b) y = 0.167

Fig. 23 Comparison of section pressure distributions between initial N2B and design configuration at Mach 0.8, altitude 35,000 ft., and AOA 3.5deg. (The right figures are zoomed windows of the left)

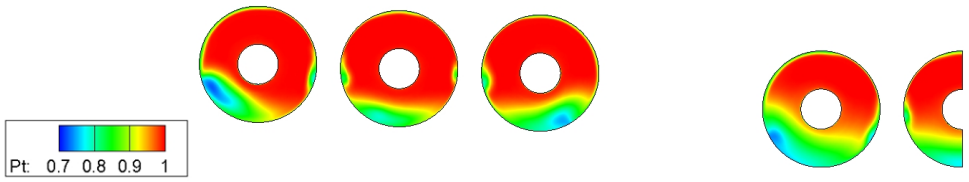

(a) Initial N2B

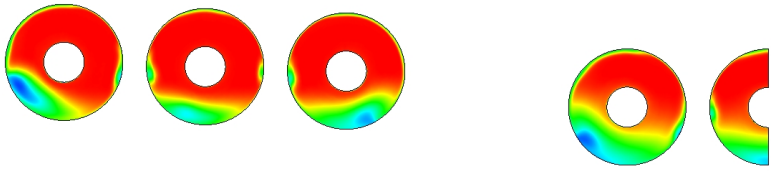

(b) Design 1

Fig.24 Normalized total pressure contours at AIPs

B. Design 2: distortion minimization

The result of the drag minimization is used as a baseline configuration for the distortion minimization. The design objective is to minimize a sum of values of the circumferential distortion indicator $DPCP_{avg}$ for the three AIP's of the side inlet (AIP1,2,3). The design condition remains the same as the flow simulation and the drag minimization: the TOC condition with a fixed angle of attack. The amount of geometric variation is restricted to be less than 10% of fan diameter. The design problem is defined as follows:

$$\text{Min} \qquad F = \sum_{i=1}^{3} \text{DPCP}_{\text{avg\_AIP}i} \tag{9}$$

$$\text{Subject to} \quad |\delta \mathbf{x}| < 10\% \text{ of fan diameter}$$

As design parameters, perturbations of control points on the diffuser surfaces are adopted. The total number of design parameters is 52 for the side inlet only, and the center inlet is not considered in the distortion design study. Variation of internal geometric shape in the diffuser of the side inlet does not have noticeable effects on the AIP's of the central inlet.

Figure 25 compares diffuser surface shapes between Design 1 and Design 2. By the Design 2, side wall shapes became curved, and the bottom surfaces are also got wavier than the Design 1 configuration.

Comparison of total pressure contours in Fig. 26 shows that the low recovery region at AIP1 is smeared out and spread into wider area by Design 2, and the lowest recovery value got increased remarkably. Also, AIP 3 shows an increment of the minimum recovery value.

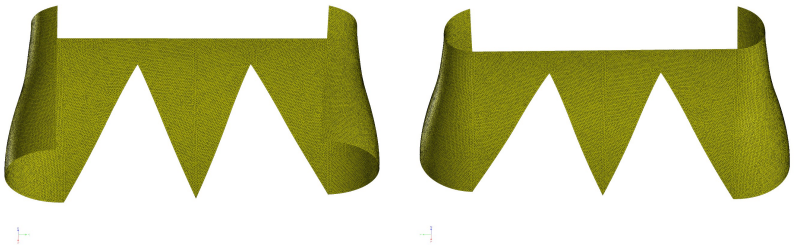

(a) Design 1 (Flows from up to down)

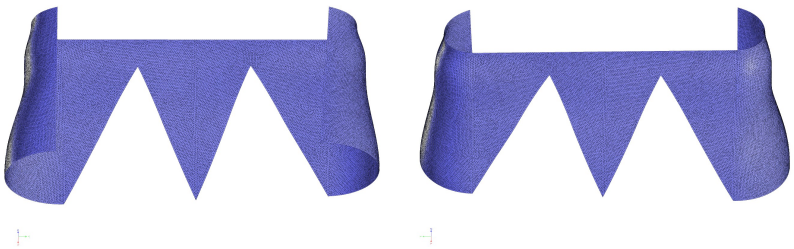

Design 2 (Flows from up to down)

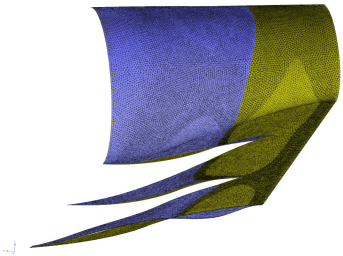

(b) Section view of the bottom surfaces. Gold is Design 1 and blue is Design 2. (Flows from right to left)

Fig. 25 Comparison of design shape change of diffuser bottom and side walls for the side inlet

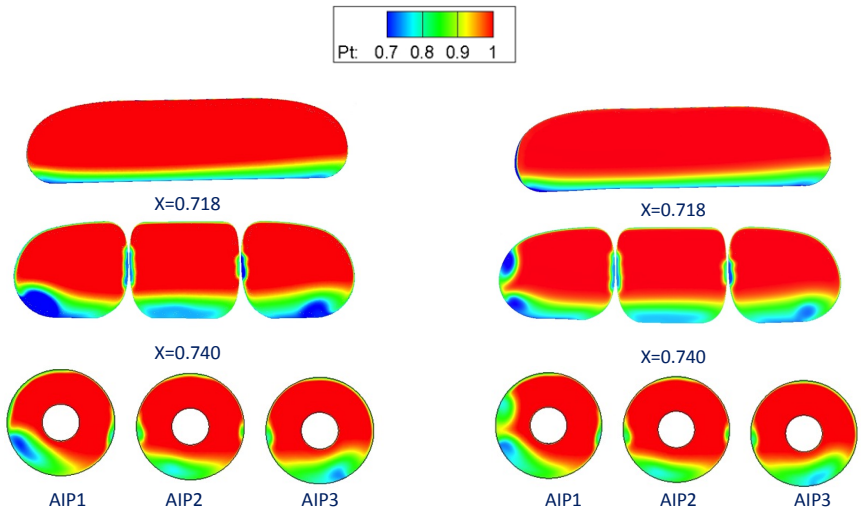

(a) Design 1 **(b) Design 2**

Fig.26 Comparison of normalized total pressure contours inside the diffuser of the side inlet for Design 1 and Design 2 configurations

Figure 27 compares distortion indicators of the initial, Design 1 and Design 2 configurations. Although design 1 has reduced the drag force remarkably, it has also increased both the distortion indicators. By the Design 2, the objective function, the sum of $DPCP_{avg}$ at AIP1, 2, and 3 is reduced by 12.0% compared to Design 1. The most amount of improvement comes from the AIP1, where $DPCP_{avg}$ is reduced by 23.9 %. DC60 shows a slightly different trend. DC60 is reduced for AIP1 and AIP2, but is increased for AIP3 by Design 2. AIP4 and AIP5 have no changes in distortion indicators by Design 2 because the distortion design is limited to the side inlet in the present study.

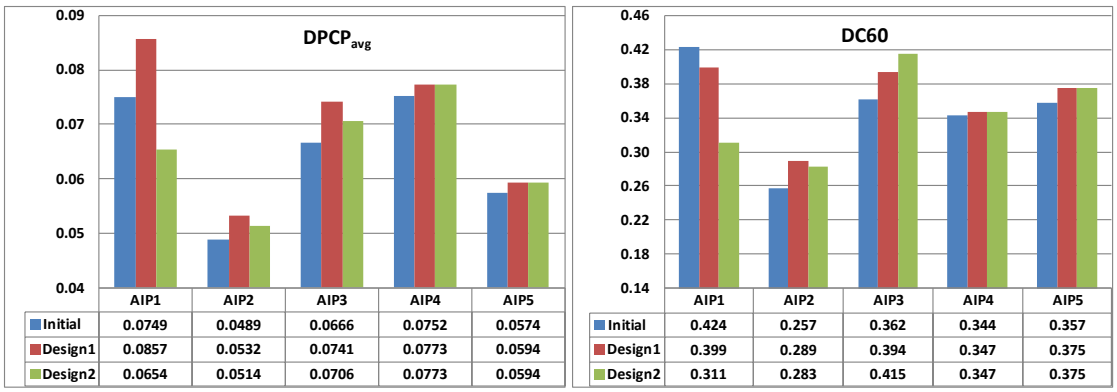

	AIP1	AIP2	AIP3	AIP4	AIP5
Initial	0.0749	0.0489	0.0666	0.0752	0.0574
Design1	0.0857	0.0532	0.0741	0.0773	0.0594
Design2	0.0654	0.0514	0.0706	0.0773	0.0594

	AIP1	AIP2	AIP3	AIP4	AIP5
Initial	0.424	0.257	0.362	0.344	0.357
Design1	0.399	0.289	0.394	0.347	0.375
Design2	0.311	0.283	0.415	0.347	0.375

Fig. 27 Comparison of distortion indicators at AIP

As shown in Fig.28, Design 1resulted in slightly reduced recovery values from the initial N2B configuration for all the five AIP's although it is very hard to tell from seeing the total pressure contours at AIP's in Fig.24. And by Design 2, the recovery is reduced at AIP1, slightly increased at AIP2, and not changed at AIP3. AIP4 and AIP5 should have no changes because the center inlet is not modified by Design 2.

Figure 29 compares lift coefficients of the clean wing, initial N2B, Design 1 and design 2 configurations. As mentioned earlier, the initial N2B has much lower lift force than the clean wing at the same angle of attack, and Design 1 has much enhanced lift force than the initial N2B. The lift of Design 2 shows little difference from that of Design 1.

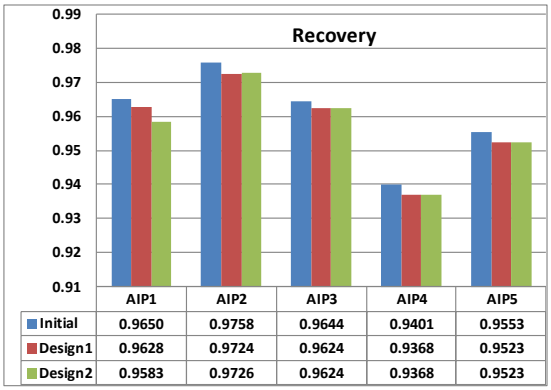

	AIP1	AIP2	AIP3	AIP4	AIP5
Initial	0.9650	0.9758	0.9644	0.9401	0.9553
Design1	0.9628	0.9724	0.9624	0.9368	0.9523
Design2	0.9583	0.9726	0.9624	0.9368	0.9523

Fig.28 Comparison of recoveries at AIP

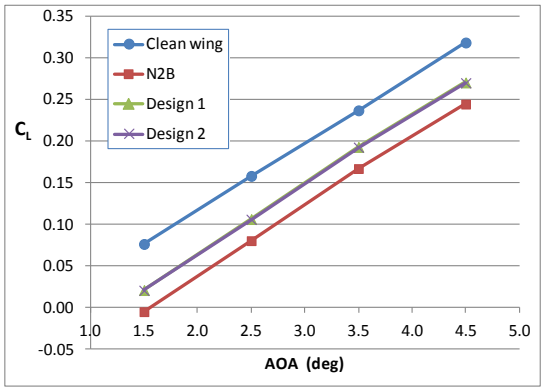

Fig.29 Comparison of lift coefficients at the TOC condition

VI. Concluding Remarks

High fidelity flow simulations were conducted for the N2B Hybrid Wing Body configuration with airframe-propulsion integration effects. Thermodynamic cycle of turbofan engines proposed for the N2B aircraft were represented by the NPSS engine models. The simulation results revealed complex flow characteristics resulting from the tightly integrated airframe-propulsion system, which are very hard to estimate *a priori* and were seen to be of considerable departure from that of a clean wing without embedded engines.

The simulation results show that strong shock waves and flow separations are occurring on the cowl surface. The pre-compression in front of the embedded engine inlet and the poor performance of the inlet cowl causes a lift deficit, which is very critical in aircraft performance. Local inflow angle effects such as side angle or incidence angle to the inlet cowl should be considered in a detailed shape design of the integrated airframe-propulsion system. The present flow simulation results on the hybrid wing body configuration are providing information and knowledge not only on the N2B aircraft but also on other HWB configurations with embedded engine concepts.

The present study also established an adjoint-based optimal shape design system for BLI inlet shape design on HWB vehicles utilizing NURBS patches for surface perturbations, a spring analogy for more drastic design changes like cowl lip shape variations, and efficient mesh modification. The current design system can be applied with various combinations of design parameters as far as the amount of design change is relatively small and topology of surface patches is not changed. Otherwise, component based Boolean operations followed by re-generation of surface and volume meshes would be required.

Shape design optimization of the inlet of the HWB configuration is conducted in two steps. The first step is a drag

minimization reshaping airframe-nacelle integration to minimize shock waves and flow separations on the cowl surfaces. The second step was a distortion minimization improving flow quality at fan faces by a design of diffuser wall surfaces. The first step resulted in remarkably improved flow characteristics on the cowl surfaces. The second step of the inlet shape design reveals a great potential of optimal shape design for distortion minimization. In a further work, various densities of design parameters for various locations of design surfaces will be tested for the distortion design.

Acknowledgements

The authors are grateful for the support by the NASA's Subsonic Fixed Wing Project of Fundamental Aeronautics Program.

References

[1]NASA Research and Technology Program and Project Management Requirements, NASA Procedural Requirements 7120.9. Appendix J. Technology Readiness Levels (TRLs), February 05, 2008.

[2]Liebeck, R. H., "Design of the Blended Wing Body Subsonic Transport," *J. Aircraft*, Vol. 41, No. 1, January-February 2004.

[3]Kawai, R. and Brown, D., "Acoustic Prediction Methodology and Test Validation for an Efficient Low-Noise Hybrid Wing Body Subsonic Transport," Phase I Final Report PWDM08-006A, NASA Contract Number NNL07AA54C, October, 2008.

[4]Hileman, J. I, Spakovszky, Z. S., Drela, M., Sargeant, M. A., Jones, A., "Airframe Design for Silent Fuel-Efficient Aircraft," *J. Aircraft*, vol.47, No.3, May-June 2010, pp. 956-969. See also AIAA Paper 2007-453, Jan., 2007.

[5]de la Rosa Blanca, E., Hall, C. A., and Crichton, D., "Challenges in the Silent Aircraft Engine Design," AIAA Paper 2007-454, Jan., 2007.

[6]Allan, B. G., Owens, L. R., and Lin, J. C., "Optimal Design of passive Flow Control for a Boundary-Layer-Ingesting Offset Inlet Using Design-of-Experiments," *AIAA 2006-1049*, January 2006.

[7]Lee, B. J., Liou, M.-S., and Kim, C., "Optimizing a Boundary-Layer-Ingesting Offset Inlet by Discrete Adjoint Approach," *AIAA J.*, Vol. 48, No.9, September 2010, pp. 2008-2016.

[8]Carter, M. B., Campbell, R. L., Pendergraft, O. C. Jr., Friedman, D. M., and Serrano, L. "Designing and Testing a Blended Wing Body with Boundary-Layer Ingestion Nacelles," *AIAA J. Aircraft*, Vol. 43, No.5, Sept.-Oct. 2006, pp. 1479-1489.

[9]Rodriguez, D. L. "Multidisciplinary Optimization Method for Designing Boundary Layer Ingestion Inlets," *AIAA J. Aircraft*, Vol. 46, No.3, May-June 2009, pp. 883-894.

[10]Tong, M., Jones, S. M., Haller, W. J., and Handschuh, R. F., "Engine Conceptual Design Studies for a Hybrid Wing Body Aircraft," NASA/TM-2009-215680, November 2009. Appears also in Turbo Expo 2009, ASME, Orlando, FL, June 8-12, 2009.

[11]NASA-Industry Cooperative Effort, "Numerical Propulsion System Simulation User Guide and Reference," Software Release NPSS 1.5.0, May 7, 2002.

[12]Litle, J. K., "Numerical Propulsion System Simulation: An Overview," NASA/TM-2000-209915.

[13]Kim, H., Kumano, T., Liou, M.-S., Povinelli, L. A., and Conners, T., "Numerical Propulsion Flow Simulation of Supersonic Inlet with Bypass Annular Duct," *J. Propulsion and Power*, Vol.27, No.1, January-February 2011. pp. 29-39.

[14]Menter, F.R, "Two-Equation Eddy-Viscosity Turbulence Models for Engineering Applications," *AIAA J.*, Vol.32, No.8, August 1994, pp.1598-1605.

[15]Spalart, P. R. and Rumsey, C., "Effective Inflow Conditions for Turbulence Models in Aerodynamic Calculations," *AIAA J.*, Vol.45, No.10, October 2007, pp.2544-2553.

[16]Sharov, D. and Nakahashi, K. "Reordering of Hybrid Unstructured Grids for Lower-Upper Symmetric

Gauss-Seidel Computations," *AIAA J.*, Vol.36, No.3, pp.484–486, 1998.

[17]Ito, Y. and Nakahashi, K., "Direct Surface Triangulation Using Stereolithography Data," *AIAA J.,* Vol. 40, No. 3, March 2002, pp. 490–496.

[18]Ito, Y., Shih, A. M., Soni, B. K. and Nakahashi, K., "Multiple Marching Direction Approach to Generate High Quality Hybrid Meshes," *AIAA J.*, Vol. 45, No. 1, January 2007, pp. 162–167.

[19]O'Brien, D. M. Jr., Calvert, M. E., Butler, S. L. "An Examination of Engine Effects on Helicopter Aeromechanics," *AHS Specialist's Conference on Aeromechanics,* San Francisco, CA, Jan. 23-25, 2008.

[20]Kim, H., Kumano, T., Liou, M.-S., Povinelli, L. and Conners, T., "Flow Simulation of Supersonic Inlet with Bypass Annular Duct," *AIAA J. Propulsion and Power*, vol. 27, No. 1, Jan-Feb. 2011, pp.29-39, See also AIAA 2010-0480, 48th AIAA Aerospace Science Meeting, Orlando, FL, Jan. 2010.

[21]Hsiao, E., Naimi, M., Lewis, J. P., Dalbey, K., Gong, Y., Tan, C., "Actuator Duct Model of Turbomachinery Components for Powered-Nacelle Navier-Stokes Calculations," *AIAA J. Propulsion and Power*, Vol.17, No.4, 2001, pp. 919-927.

[22]Chima, R.V., "Rapid Calculations of Three-Dimensional Inlet/Fan Interaction," NASA Fundamental Aeronautics 2007 Annual Meeting, Oct. 30 - Nov. 1, 2007, New Orleans, LA.

[23]*Gas Turbine Engine Inlet Flow Distortion*, Society of Automotive Engineers, Rept. ARP-1420, March 1978.

[24]Hercock, R.G. and Williams, D. D., "Aerodynamic Response," Paper 3, AGARD Lecture Series 72, 1974. (DC60)

[25]Jameson, A., "Aerodynamic Shape Optimization Using the Adjoint Method," *Lecture series*, Von Karman Institute for Fluid Dynamics, Feb. 2003.

[26]Nielson, E. J., and Anderson, W. K., "Aerodynamic Design Optimization on Unstructured Meshes Using the Navier-Stokes Equations," *AIAA J.* Vol.37, No.11, 1999, pp1411-1419.

[27]Mavriplis, D. J. "A Discrete Adjoint-Based Approach for Optimization Problems on Three-Dimensional Unstructured Meshes," *AIAA J.* Vol. 45, No. 4, pp. 740-750, April 2007.

[28]Kim, H., Sasaki, D., Obayashi, S., and Nakahashi, K., "Aerodynamic Optimization of Supersonic Transport Wing Using Unstructured Adjoint Method," *AIAA J.* Vol. 39, No. 6, pp. 1011-1020, June 2001.

[29]Kim, H. and Nakahashi, K., "Unstructured Adjoint Method for Navier-Stokes Equations," *JSME International J. Series B,* Vol. 48, No.2, pp. 202-207, May 2005.

[30]Y. Saad and M.H. Schultz, "GMRES: A generalized minimal residual algorithm for solving nonsymmetric linear systems", *SIAM J. Sci. Stat. Comput.*, **7**:856-869, 1986.

[31]Lepine, J., Guibault, F., Trepanier, J.-Y., Pepini, F., "Optimizaed Nonuniform Rational B-Spline Geometrical Representation for Aerodynamic Design of Wings, " *AIAA J.*, Vol. 39, No.11, 2001, pp.2033-2041.

[33] Vanderplaats, G. N., *Numerical Optimization Techniques for Engineering Design: With Applications*, pp. 88-89, McGraw Hill, N.Y., 1984.

[34]Kawai, R. T., Friedman, D. M., and Serrano, L. "Blended Wing Body (BWB) Boundary Layer Ingestion (BLI) Inlet Configuration and System Studies," NASA CR-2006-214534, December, 2006.

[34]Takenaka, K., Hatanaka K. and Nakahashi, K., "Efficient Aerodynamic Design of Complex Configurations by Patch-Surface Approach," *J. Aircraft*, Vol. 48, No.5, September-October 2011, pp. 1473-1481.

[35]Owens, L. R., Allan, B. G., and Gorton, S. A., " Boundary-Layer-Ingesting Inlet Flow Control," *AIAA J. Aircraft*, Vol. 45, No.4, July-August 2008, pp. 1431-1440.

[36]Allan, B. G. and Owens, L. R., "Numerical Modeling of Flow Control in a Boundary-Layer-Ingesting Offset Inlet Diffuser at Transonic Mach Numbers," AIAA 2006-0845, 44th AIAA Aerospace Science Meeting, January 2006, Reno, NV.

[37]Johnson, B. C., Webster, R. S., and Sreenivas, K., "A Numerical Investigation of S-Duct Flows with Boundary-Layer Ingestion," AIAA 2010-0841, 48th AIAA Aerospace Science Meeting, January 2006, Orlando, FL.

APPENDIX: Validation of the Flow Solver for Boundary Ingestion Offset Inlet Diffuser

For validation of the flow solver on configurations including BLI offset inlets, flow simulations are conducted for a flush-mounted offset inlet shown in Fig.A1 and compared to the experimental results obtained by Owens et al. [35] at NASA Langley's 0.3-Meter Transonic Cryogenic Tunnel, in which the inlet was flush-mounted on the tunnel sidewall.

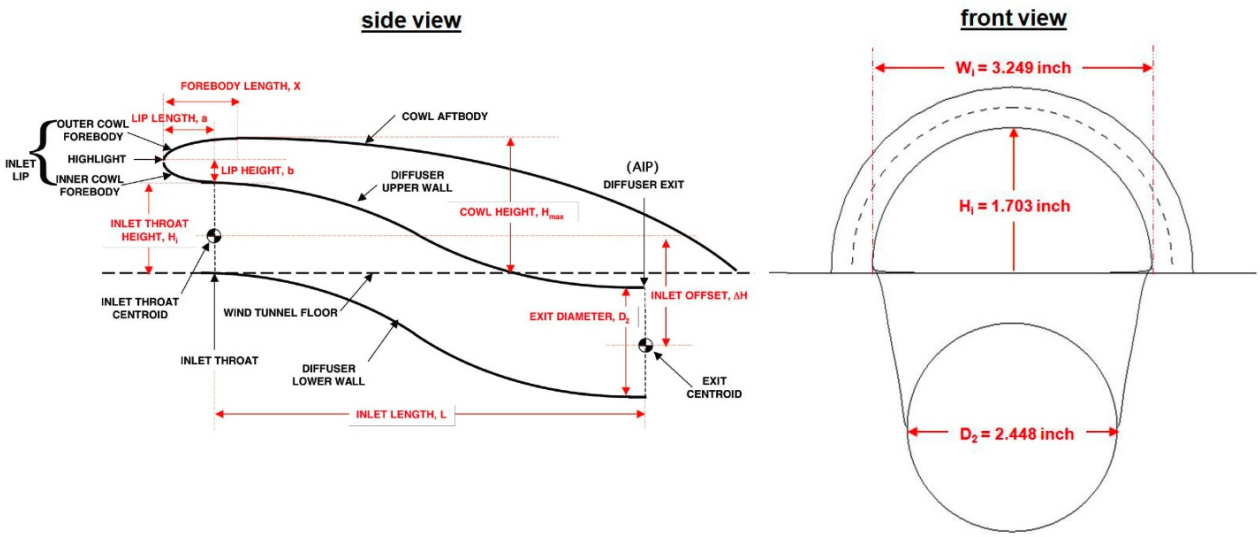

(a) Side and front views

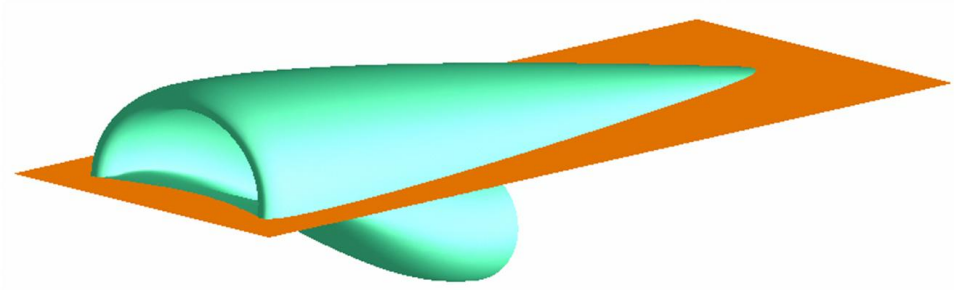

(b) CAD surface representation

Fig.A1 BLI offset inlet configuration: Inlet A model [35]

Computational mesh for the BLI offset inlet is shown in Fig.A2. Outer boundaries are composed of inflow, side, top and outlflow planes. The outer boundaries are set as freestream boundary conditions. The side, top and outflow planes respectively are 50 inches away from the inlet throat centroid. The viscous flat plate length ahead of the inlet is adjusted to match the experimental bondary layer thickness at the inlet. The total number of mesh points is about 10 million, and first nodes off the viscous wall are clustered to the wall so that maximum y+ value is less than 2.

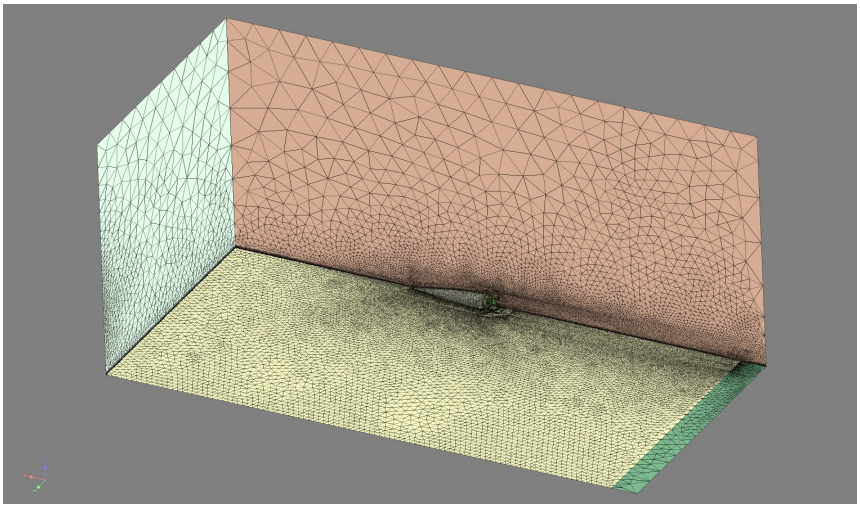

(a) Surface mesh for the computational domain

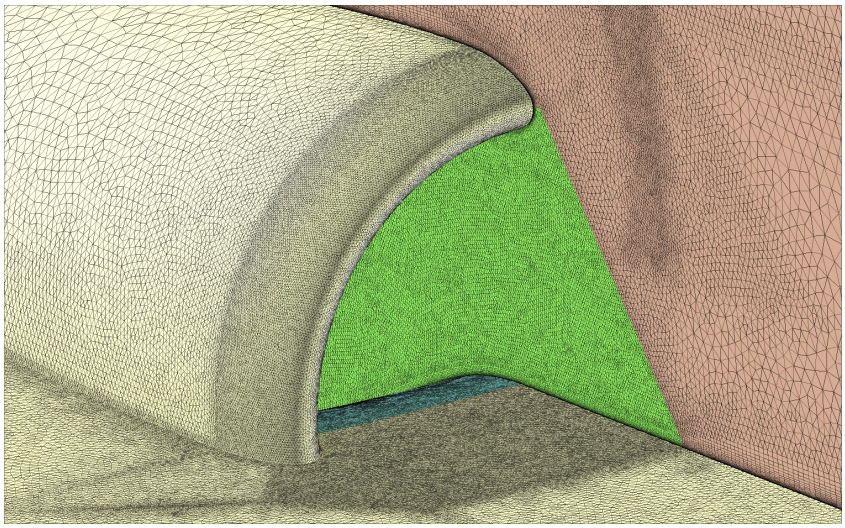

(c) Zoomed view near the inlet entrance

Fig.A2 Computational mesh

To ensure the numerical simulations are conducted at the same flow condition as the wind tunnel testing of the BLI offset inlet, several parameters need to be matched; the freestream Mach number, the Reynolds number, the boundary layer profile at the inlet, and the inlet mass flow rate. As mentioned earlier, the height of boundary layer profile is matched by adjusting the flat plate length ahead of the inlet. The inlet mass flow rate is controlled by varying a static back pressure at the AIP. The freemstream Mach number is 0.85 and the Reynolds number based on AIP diameter, $Re_D = 3.8\times10^6$, which is consistent with the experimental flow conditions in Ref.17, where the Mach number was held at a constant 0.85 upstream of the inlet. Freestream boundary conditions for turbulence valriables are set as $k_\infty/u_\infty^2 = 10^{-6},\ \omega_\infty L/u_\infty = 5$ following recommendations given in Ref.12.

Because the flow field has adverse pressure gradient as the flat plate boundary layer flow approaches the inlet entrance, just matching the boundary layer height does not necessarily mean the same boundary layer is ingested into the inlet. The amount of adverse pressure gradient due to the local flow conditions in the test section of the wind tunnel would affect more the detailed shape of the boundary layer profile ahead of the inlet. Figure A3 shows velocity profiles by the present numerical simulations and experimental results at the boundary layer rake location. The computaional velocity profile in a solid line has slightly higher verlocity in the bottom part of the boundary layer, which is consistent with other CFD analysis results in Ref. 19. Lee et al. [7] compared boundary layer velocity profiles for $Re_D = 2.2\times10^6$ and 3.8×10^6 and found the lower Reynolds number, $Re_D = 2.2\times10^6$, results in a closer velocity profile to the

experimental profile than the higher Reynolds number $Re_D = 3.8\times10^6$. Also, $Re_D = 2.2\times10^6$ results in better comparisons for pressure distributions with experimental data than $Re_D = 3.8\times10^6$ does. Thus, it is deemed that the extent of matching the experimental boundary layer profile affects accuracy of computation of the pressure distributions inside the duct.

CFD simulations for the BLI offset inlet test case in literature often uses a lower Reynolds number than the experimental Reynolds number $Re_D = 3.8\times10^6$ probably to match the boundary layer velocity profile more closely to the experimental data. (e.g. $Re_D = 2.2\times10^6$ in Ref.19) However, the use of a lower Reynolds number also results in significantly lower total pressure recoveries at AIP [7, 36]. In this study, instead of changing the Reynolds number, the static back pressure of the outflow boundary plane is adjusted to match the computational and experimental velocity profiles in the boundary layer as closely as possible. In the case of back pressure adjustment, the side and top boundary surfaces are treated as inviscid walls. In Fig.A3, the graph in a dashed line shows the velocity profile obtained by the present study with adjustment of the back pressure, which is lower than the freestream pressure. Note that the outflow plane and AIP are different exit boundary planes.

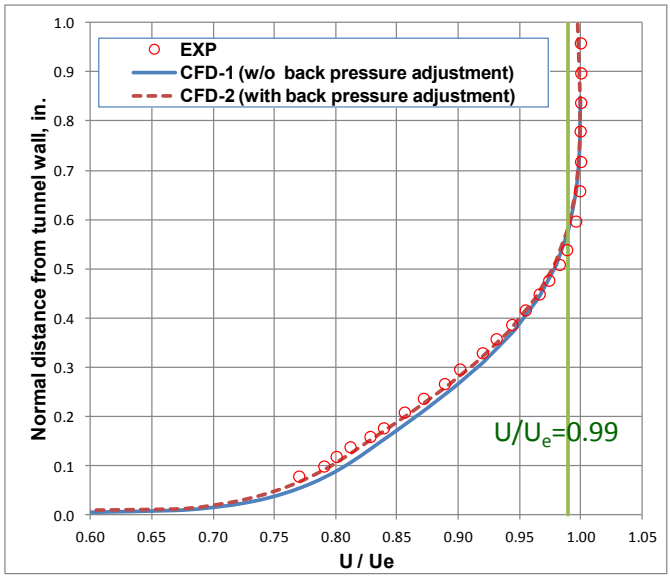

Fig.A3 Comparison of boundary layer profiles.
Exp: M_∞=0.843, Re_D=3.3×10^6, CFD: M_∞=0.850, Re_D=3.8×10^6
CFD-1: present simulation results *without* back pressure adjustment
CFD-2: present simulation results *with* back pressure adjustment

Figure A4 compares inlet centerline pressures from experimental and the present CFD results. The CFD results include two sets of data without and with the back pressure adjustment for boundary layer profile matching. The pressure distribution without the back pressure correction deviates upward from the experimental data. Meanwhile the pressure with the back pressure adjustment shows a very good comparison both on upper and lower surfaces inside the inlet.

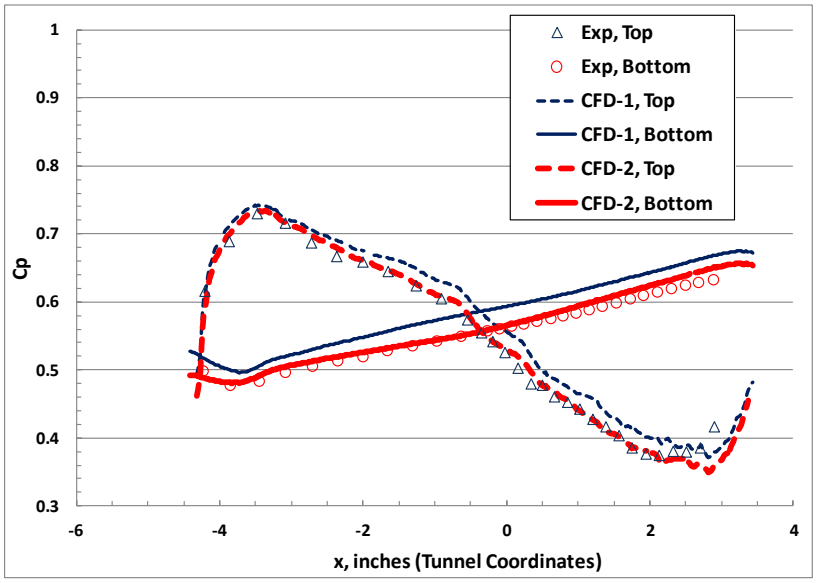

Fig.A4 Comparison of inlet centerline pressure on the top and bottom of the BLI inlet. M_∞=0.85, $Re_D = 3.8\times10^6$, Experimental data: wall correction (See Fig. A3 for definitions of CFD-1 and CFD-2)

The inlet mass flow rate was represented by the area ratio A_0/A_c where A_0 is the area in the freestream flow that corresponds to the mass flow rate fed into the inlet:

$$\rho_0 U_0 A_0 = \rho_c U_c A_c \tag{A1}$$

The inlet capture area, A_c, is defined by the inlet section area at the cowl highlight. As for an indicator for flow distortion at AIP, the SAE circumferential distortion descriptor, $DPCP_{avg}$ [23] is used to compare with results of experimental and other numerical studies in the literature.

The inlet performance parameters obtained by the present flow simulations are compared with the experimental data in Table A1. The present results show good comparisons with experimental and other CFD results. Finally, contours of the local total pressure normalized by the freestream value are compared for experimental and other CFD results. The present results are calculating the location of the minimum total pressure region slightly higher than other results. Other than that, the overall trend is well simulated by the present CFD code.

Table A1 Comparison of performance parameters of the BLI inlet (See Fig. A3 for definitions of CFD-1 and CFD-2)

	A_0/A_c	Distortion ($DPCP_{avg}$)	Pressure recovery	Reynolds number Re_D
Experiment [35]	**0.534**	**0.054**	**0.952**	**3.8×10^6**
Present CFD-1	**0.536**	**0.052**	**0.948**	**3.8×10^6**
Present CFD-2	**0.532**	**0.054**	**0.941**	**3.8×10^6**
CFD [7]	**0.533**	**0.060**	**0.956**	**3.8×10^6**
CFD [7]	**0.527**	**0.063**	**0.943**	**2.2×10^6**
CFD [36]	**0.537**	**0.054**	**0.943**	**2.2×10^6**
CFD [37]	**N/A**	**0.056**	**0.934**	**1.8×10^6**

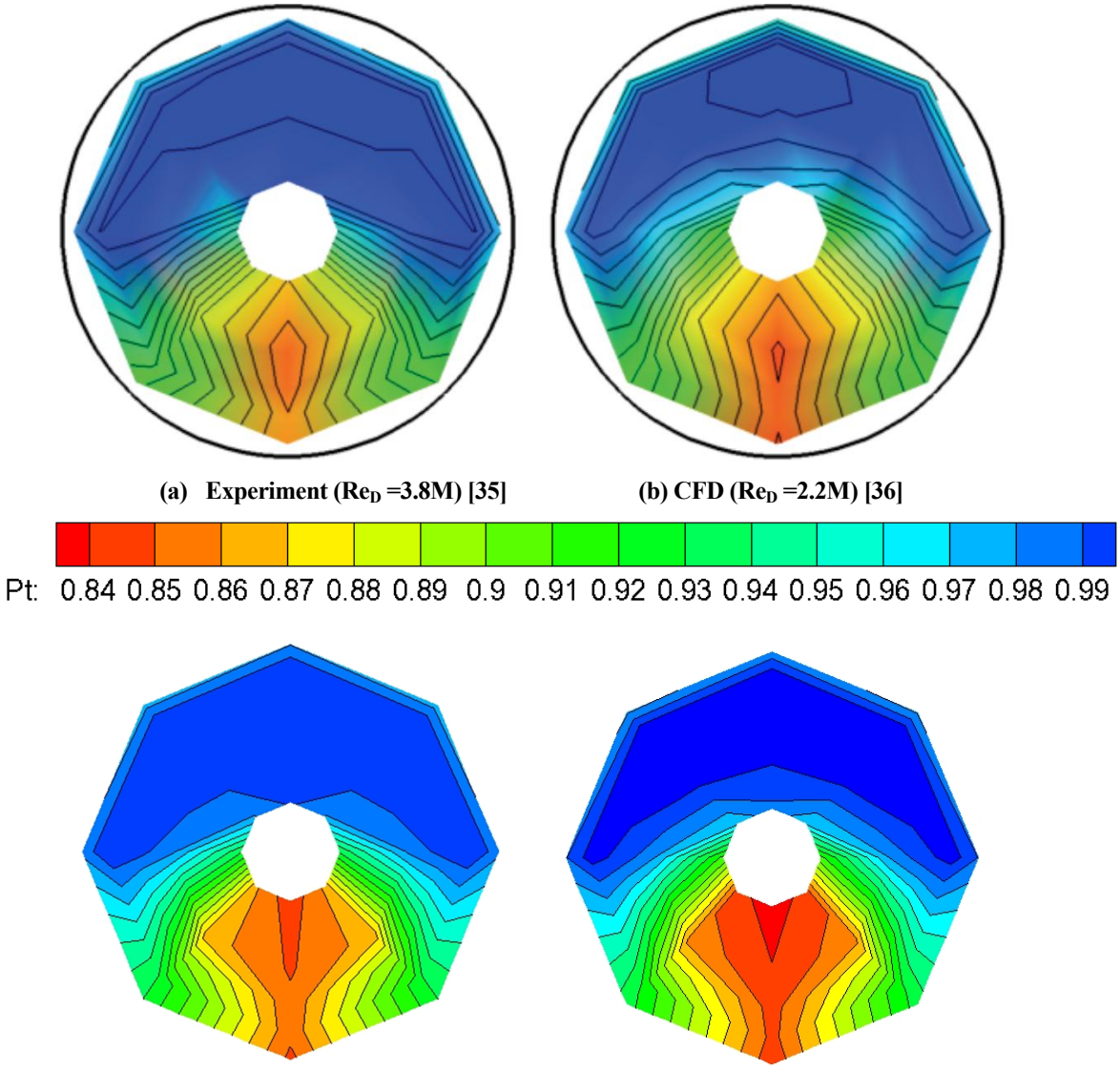

(a) Experiment (Re_D =3.8M) [35] **(b) CFD (Re_D =2.2M) [36]**

(c) Present CFD-1 (Re_D =3.8M) **(d) Present CFD-2 (Re_D =3.8M)**

Fig.A5 Comparison of total pressure contours at AIP (M_∞=0.85)
(See Fig. A3 for definitions of CFD-1 and CFD-2)